Widespread Exposures of Extensive Clean Shallow Ice in the Mid-Latitudes of Mars

Colin M Dundas, Michael T Mellon, Susan J. Conway, Ingrid J Daubar, Kaj E Williams, Lujendra Ojha, James J Wray, Ali M Bramson, Shane Byrne, Alfred S Mcewen, et al.

Widespread Exposures of Extensive Clean Shallow Ice in the Mid-Latitudes of Mars

Colin M. Dundas[a] *

Michael T. Mellon[b]

Susan J. Conway[c]

Ingrid J. Daubar[d]

Kaj E. Williams[a]

Lujendra Ojha[e]

James J. Wray[f]

Ali M. Bramson[g]

Shane Byrne[h]

Alfred S. McEwen[h]

Liliya V. Posiolova[i]

Gunnar Speth[i]

Donna Viola[j]

Margaret E. Landis[k]

Gareth A. Morgan[l]

Asmin V. Pathare[l]

[a]U.S. Geological Survey, Astrogeology Science Center, 2255 N. Gemini Dr., Flagstaff, AZ 86001, USA (cdundas@usgs.gov).

[b]Center for Astrophysics and Planetary Science, Cornell University, Ithaca, NY, USA.

[c]Laboratoire de Planétologie et Géodynamique CNRS UMR 6112, Université de Nantes, France.

[d]Department of Earth, Environmental, and Planetary Sciences, Brown University, Providence, RI, USA.

[e]Department of Earth and Planetary Sciences, Rutgers University, Piscataway, NJ, USA.

[f]School of Earth and Atmospheric Sciences, Georgia Institute of Technology, Atlanta, GA, USA.

[g]Department of Earth, Atmospheric, and Planetary Sciences, Purdue University, West Lafayette, IN, USA.

[h]Lunar and Planetary Laboratory, The University of Arizona, Tucson, AZ, USA.

[i]Malin Space Science Systems, San Diego, CA, USA.

[j]NASA Ames Research Center, Moffett Field, CA, USA.

[k]Laboratory for Atmospheric and Space Physics, University of Colorado, Boulder, CO, USA.

[l]Planetary Science Institute, Tucson, AZ, USA.

*Corresponding author.

Abstract

Although ice in the Martian mid-latitudes is typically covered by a layer of dust or regolith, it is exposed in some locations by fresh impact craters or in erosional scarps. In both cases, the exposed ice is massive or excess ice with a low lithic content. We find that erosional scarps occur between 50–61° north and south latitude and that they are concentrated in and near Milankovič crater in the northern hemisphere and southeast of the Hellas basin in the southern hemisphere. These may represent locations of particularly thick or clean bodies of ice. Pits created by retreat of the scarps represent sublimation-thermokarst landforms that evolve in a manner distinct from other ice-loss landforms on Mars. New impact craters reveal that clean subsurface ice is widespread at middle and high latitudes in both hemispheres at depths less than 1 meter. Both the depth to ice and the ice content appear to exhibit significant variability over tens to hundreds of meters. The lowest-latitude exposed ice is near 39 °N and is at the edge of a region where impact exposures between 40–50 °N are common, consistent with other indications of a high ice content. This lowest-latitude ice may be currently unstable and subliming. Impact craters on lineated valley fill excavate ice blocks that may represent the top of debris-covered glacial ice. Together, these landforms indicate widespread, clean subsurface ice at middle latitudes on Mars. The distribution and properties of this ice could provide information about past climate conditions.

Plain Language Summary

Ice occurs at the surface near the north and south poles of Mars, but in the mid-latitudes it is usually buried beneath rocks and dust. Impact craters and erosion expose

the ice in some places. At these locations, the ice is generally clean, with little dust or rocky material embedded within it, in contrast with pore ice filling in voids in soil. The erosional exposures are concentrated in and near Milankovič crater in the northern hemisphere and southeast of the Hellas basin in the southern hemisphere and occur at a narrow range of latitudes. These may be locations of particularly thick, clean ice. Impact craters reveal that some amount of such subsurface ice is widespread. The craters help to define the lowest latitude where ice is present and how deeply it is buried, which could provide information about the history of the climate on Mars.

1. Introduction

One of the key needs identified by the Mars science community is the inventory and characterization of non-polar near-surface ice (Smith et al., 2018; MEPAG ICE-SAG Report, 2019). This is a fundamental question for determining the near-surface H_2O abundance on Mars and the processes by which it is transported, deposited, and modified. Theory indicates that ice stability is controlled by temperature and the atmospheric water vapor content (e.g., Leighton and Murray, 1966; Mellon and Jakosky, 1993; 1995; Mellon et al., 2004; Schorghofer and Aharonson, 2005; Chamberlain and Boynton, 2007; Steele et al., 2017), and thus a stability boundary varies over time depending on the history of those parameters. This climatic change in turn is governed by variations in Mars' orbit and obliquity (e.g., Murray et al., 1973; Ward, 1973; Laskar et al., 2004). Small adjustments of the ice-table depth in response to climate changes can occur within hundreds of years even in the presence of salt crusts or other plausible diffusion barriers (e.g., Mellon et al., 2004; Hudson and Aharonson, 2008). However, thick bodies of ice might survive through intervals of instability (e.g., Schorghofer and Forget, 2012; Bramson et al., 2017). There is evidence that shallow (<10 m) mid-latitude ice has survived for tens of millions of years (Viola et al., 2015) and debris-covered glaciers have an estimated mean age of 110 Ma since the last major ice accumulation (Fassett et al., 2014). Thus the distribution of ice is influenced by its stability in the geologically recent past as well as the present. Additionally, early expectations were that most subsurface ice would simply fill in the pore space of the regolith (e.g., Squyres and Carr, 1986; Mellon and Jakosky, 1993). However, many lines of evidence (e.g., Boynton et al., 2002; Mellon et al., 2009; Smith et al., 2009; Mouginot et al., 2010; Conway and Balme, 2014;

Bramson et al., 2015; Dundas et al., 2015; Stuurman et al., 2016; Pathare et al., 2018) now point to the widespread occurrence of excess or massive ice (terminology per van Everdingen (1998)) rather than pore ice, requiring additional processes such as snowfall (e.g., Madeleine et al., 2009; 2014), thermal cycling to enhance porosity (Fisher, 2005), or migration of thin liquid films to generate ice lenses (e.g., Sizemore et al., 2015). Hence, assessing the distribution, concentration, and structure of ground ice is vital for understanding recent Martian climate and its variations.

Ground ice in the Martian mid-latitudes is widespread, but almost always underneath a desiccated protective layer of dry permafrost. This structure was first predicted by Leighton and Murray (1966) and subsequently confirmed by refined models (e.g., Mellon et al., 2004; Schorghofer and Aharonson, 2005; Chamberlain and Boynton, 2007; Steele et al., 2017). Observations from gamma-ray and neutron spectroscopy (e.g., Boynton et al., 2002; Mitrofanov et al., 2018; Pathare et al., 2018), thermal emission (e.g., Bandfield, 2007; Bandfield and Feldman, 2008; Piqueux et al., 2019), and direct excavation by the Phoenix lander (Mellon et al., 2009; Smith et al., 2009) confirm this structure. Unfortunately, the desiccated layer shields the ice from direct view, and exposed ice is expected to sublimate rapidly at mid-latitudes and create a new covering deposit, so the ice is usually concealed beneath dust and regolith.

Natural exposures provide local information about the current state of subsurface ice, such as the ice content, geographic distribution, and layering at each site. There are two main categories of natural exposure. Small craters (Fig. 1a) pierce the desiccated cover and create temporary exposures or excavate formerly buried ice onto their ejecta blankets (Byrne et al., 2009; Dundas et al., 2014). These constitute high-resolution point

samples of the ice table and provide a valuable data set for comparison with less-direct, lower-resolution approaches to understanding the distribution of ice. However, these craters are small and shallow features, and the impact events also modify the ice relative to its baseline state. Direct, high-resolution vertical information on undisturbed mid-latitude ice structure was minimal until the discovery of scarp exposures (Fig. 1b) cutting through the ice (Dundas et al., 2018). The scarps are kilometers long, tens of meters high, and expose cross sections through the ice, revealing layering and unconformities. This ice was interpreted as sintered snow with a very low lithic content, and indications of glacial flow exist at one location. Rocks (>50 cm diameter) fell out of one of the scarps over three Mars years, suggesting ongoing sublimation, which was also indicated by weakening of H_2O spectral absorption features over the course of the summer (Dundas et al., 2018). In addition to the scarps and craters, exposed ice has been reported in some gully alcoves where it may be exposed by active erosion (Dundas et al., 2019; Khuller and Christensen, 2019), but this process has not been studied in depth.

The scarps are incised in surface-mantling deposits. Latitude-dependent mantle deposits were first observed by Mariner 9 (Soderblom et al., 1973). They were initially thought to be aeolian dust deposits, but higher-resolution imaging provided evidence that they contain ice (Mustard et al., 2001), in some cases forming thick units with a high ice content (Conway and Balme, 2014). Layering indicates deposition in multiple distinct episodes (Schon et al., 2009). Polygonal cracking visible in some of these units (e.g., Mangold, 2005; Levy et al., 2009a) indicates a structural integrity that is best interpreted as thermal contraction cracking of solid ice or ice-cemented regolith. These surface-mantling deposits are now widely thought to have been deposited as mixtures of snow or

frost and dust (in unknown and probably variable proportions) within the last few million years during periods when Mars' axial tilt was higher than at present (e.g., Mustard et al., 2001; Head et al., 2003; Schon et al., 2009; Madeleine et al., 2014).

Dundas et al. (2018) documented seven scarp exposure sites in the southern hemisphere and one cluster in Milankovič crater in the north; Harish et al. (2020) reported two additional scarps in the northern hemisphere. However, neither conducted a comprehensive survey. Additionally, the number of known ice-exposing craters has more than doubled since publication of Dundas et al. (2014). This work reports an assessment of the locations and properties of ice-exposing scarps in current data in both the northern and southern mid-latitudes and reports on the expanded data set of icy craters.

2. Methods

2.1. Data

The data sets used for this work included Thermal Emission Imaging System (THEMIS; Christensen et al., 2004) Daytime Infrared mosaics, Context Camera (CTX; Malin et al., 2007) images, and High Resolution Imaging Science Experiment (HiRISE; McEwen et al., 2007) images. The THEMIS products use daytime infrared observations and provide near-global mosaics at 100 m/pix (Fergason et al., 2019). CTX images have near-global coverage at 6 m/pix. HiRISE images reprojected to 25 or 50 cm/pix cover only a small fraction of the surface and include a central swath with two additional colors (from blue-green and near-infrared filters) within the wider red-filter image. These images were often targeted to center on the features studied here. We used HiRISE data through Mars Reconnaissance Orbiter orbit 64,199 for study of icy craters and through

168 orbit 66899 for icy scarps. We also inspected data from the Compact Reconnaissance
169 Imaging Spectrometer for Mars (CRISM; Murchie et al., 2007) where available. CRISM
170 is a visible and near-infrared spectrometer, which can provide more definitive evidence
171 for water ice than our other data sets, but observations are spatially limited and often do
172 not include the near-infrared wavelengths that provide the strongest evidence for ice. We
173 followed the same CRISM processing techniques used in Dundas et al. (2018).
174 Most HiRISE images include a near-infrared channel, so they do not detect the
175 same wavelengths as the human eye. Thus when displayed in color, they do not show true
176 colors. In the enhanced-color images shown in the figures herein (which are from
177 standard Reduced Data Records), the near-infrared filter data are displayed as red, the red
178 filter data are displayed as green, and the blue-green filter data are displayed as blue, and
179 the images are stretched to show local contrast and emphasize color variations; this is
180 standard procedure for HiRISE color products (Delamere et al., 2010). The stretch is
181 scene dependent for each observation, so conclusions about the apparent color of features
182 in different images depend on the scene having a similar range of colors and shadows.
183 This is often roughly true on Mars, where surface dust tends to be uniformly reddish.
184 However, differences in topography, atmospheric dust content, illumination, and
185 sublimation of ice can produce apparent differences in color between images as well as
186 color changes in unchanged parts of the surface when comparing images of the same site.
187 Both raw HiRISE data and calibrated top-of-atmosphere reflectance for each channel are
188 available via the Planetary Data System.
189 Materials that appear blue in stretched images may have a reddish true color but
190 are brighter than their surroundings in the HiRISE blue-green channel. Material that

191 appears white is brighter in all three channels, but generally not white in true color. We
192 refer to these enhanced colors as “relatively blue” or “relatively white” in the text below.
193 Relatively blue or relatively white coloration is not diagnostic of exposed ice (notably,
194 mafic materials including basaltic sand also appear relatively blue (Keszthelyi et al.,
195 2008; Delamere et al., 2010)). However, we considered the combination of a relatively
196 blue or relatively white color closely associated with the distinctive morphology of a
197 scarp or new crater sufficient to classify a feature as an ice exposure with a high degree
198 of confidence. Changes over time often support the presence of ice, as described below.
199
200 *2.2. Ice-Exposing Scarps*
201 We conducted a survey of the distribution of ice-exposing scarps with the
202 properties described by Dundas et al. (2018). We searched the THEMIS Daytime Infrared
203 controlled mosaics (Fergason et al., 2019) at latitudes equatorward of 65 °N/S and the
204 uncontrolled global mosaic version 12.0 (e.g., Edwards et al., 2011) poleward of 65 °N/S.
205 In the southern hemisphere, we searched latitudes 45–70 °S (planetocentric), and
206 observed scarps only between 50–61 °S. Based on the results of this search, we limited
207 the northern-hemisphere survey to 45–65 °N. All scarps identified in the northern
208 hemisphere were between 53–59 °N, indicating that these bounds were sufficiently wide.
209 Further support for these bounds is provided by Vincendon et al. (2010), who searched
210 CRISM data and found no exposed perennial ground ice between 45 °S and 50 °N. We
211 looked for irregular pits greater than a few hundred meters across and checked candidates
212 using images from CTX to look for the main identifying characteristic of ice-exposing
213 scarps: an approximately straight, smooth, sharp-edged, pole-facing scarp (Fig. 1b).

214 Candidates possessing such a scarp were classified as probable if no HiRISE color data
215 were available or considered confirmed if they displayed a distinct relatively blue
216 coloration in HiRISE images. In some of the cases from Dundas et al. (2018), spectral
217 evidence provides additional confirmation of water ice, but CRISM data are often not
218 available. An additional requirement was that coloration was present in late spring or
219 summer (no earlier than L_s=70° in the north or L_s=250° in the south, although in most
220 cases color data exist from after the solstice), to rule out lingering seasonal frost. The
221 precise duration of seasonal frost depends on latitude, slope, aspect, and substrate (*cf.*
222 Vincendon et al., 2010; Dundas et al., 2019) but these bounds make seasonal frost
223 unlikely. Some sites were classified as confirmed but marginal. In these cases, the
224 morphology matched other scarps, but the coloration was weak or only occurred on a
225 small part of the scarp (Fig. 2a). Most scarps identified as candidates based on
226 morphology were confirmed to have at least some relatively blue coloration (in the cases
227 where HiRISE images exist), but some, particularly in Milankovič crater (Fig. 2b), have
228 coloration matching the surrounding terrain. The latter are likely to be exposures that are
229 partially or completely covered by an opaque coating of dust or debris, which is likely
230 thin since the morphology remains sharp. Alternatively, the ice at such scarps might
231 contain sufficient lithic material to suppress the coloration. Users of this data set may be
232 able to treat the probable scarps as confirmed if future HiRISE or other observations meet
233 the color criteria outlined above or yield spectral evidence of ice.

234 We considered the possibility that the scarps could be locations of year-round
235 frost stability rather than exposed subsurface ice. Frost on steep (~30°) mid-latitude
236 slopes such as crater walls near 45° latitude survives until L_S~40° in the north and

237 L_S~180° in the south; near 55°, it persists until L_S~50° and L_S~210°, respectively
238 (Vincendon et al., 2010; Dundas et al., 2019). Near the poles H_2O frost survives into
239 summer on level ground (e.g., Appéré et al., 2011) and the very steep pole-facing scarps
240 have insolation roughly equivalent to the poles, although they receive more re-radiated
241 heat from other slopes. However, the scarps are erosional features, as they incise into and
242 remove surface material and have scarp-parallel ridges indicating past positions (Dundas
243 et al., 2018). Blocks falling from one scarp indicate an ongoing average retreat rate of
244 millimeters per Mars year (Dundas et al., 2018) and the same processes should act on
245 other scarps, which lack embedded rocks. Despite this, scarps retain relatively blue
246 coloration through the summer. Although some scarps possibly reach an equilibrium state
247 or even aggrade, the evidence that the scarps begin as erosional features, are actively
248 retreating at present, and yet retain the coloration of ice year-round is inconsistent with
249 persistent frost; the existence of morphologically identical scarps without icy coloration
250 also indicates that the scarp topography does not produce long-lived frost. Additionally,
251 CRISM band depth ratios at one scarp suggest coarse-grained ice rather than fine-grained
252 frost. Finally, scarp temperatures rise above the H_2O frost point (Dundas et al., 2018).
253 Thus, although there might be occasional cases of persistent frost, exposed ice is the
254 dominant explanation.

255 The quality and completeness of the THEMIS mosaics are generally good, and
256 the area where scarp pits might have been obscured or lost in data gaps is small. We also
257 spot-checked many patches with deep shading from topography by examining CTX
258 images and did not find any examples of pits or scarps hidden in this way. We used CTX
259 data to more closely examine pits and scarps found in THEMIS mosaics that appeared

consistent with the morphological criteria noted above. Those features are best seen when kilometer-scale and larger, but smaller pits that appeared to match the morphology were also inspected. Examination of hundreds of smaller or marginal-quality candidates gives us confidence that the above criteria were effective in identifying scarps. Examining every single pit or slope in the THEMIS-surveyed area at CTX resolution was not practical. In regions of dense pitting such as scalloped terrain, we inspected those several-hundred-meter scale features that appeared particularly sharp and distinct in the THEMIS mosaics, and in the course of this survey we also examined large numbers of other pits and slopes. This examination was sufficient to demonstrate that few scarps are not part of the pits that are distinctive in the THEMIS IR mosaics, although some exist. Additionally, survey results demonstrate that some scarps display gradations in morphology. In aggregate, this survey likely includes nearly all sharply defined ice-exposing scarps in the surveyed latitude zones that are near kilometer scale and larger. This completeness scale is not well defined, but we estimate that it is between 500 meters and 1 kilometer. Some smaller and less well-defined exposures are included here, but more probably remain to be discovered. The two scarps reported by Harish et al. (2020) were independently identified by our survey, supporting its effectiveness in identifying scarps at these scales.

We measured scarp morphometric data in near-nadir HiRISE images. Orthorectified images are not available for most sites, so precise geometric correction was not possible and all dimensions are approximate, but for typical near-nadir viewing geometry the distortion is small except on steep topography. Morphometric data include the end-to-end straight-line distance, the greatest plan-view width, the estimated retreat

distance (between the scarp face and any geomorphic indication of the initiation point), and the orientation of a line connecting the scarp endpoints.

Only one site has a high-resolution digital terrain model (DTM) (Dundas et al., 2018). For some sites where appropriate images exist, we made slope estimates using the shadow method of Dundas (2017b). This method takes advantage of the fact that for a given Sun position and slope azimuth, there is a unique slope angle at which the slope begins to cast shadows. We identified locations on the brink of self-shadowing by selecting sections of slope with patchy coverage by local shadows. This method has two major limitations. First, for any given Sun position it can only indicate particular slope/aspect combinations, which may not be representative of the whole scarp and certainly do not capture local variability. This could also result in biases when comparing between sites, since the available images might favor different slope/aspect combinations at different sites. Second, the method requires manual estimation of the downhill direction. This is challenging, especially on curved slopes, and results in large uncertainties. This method gives good results when applied to the scarp with a corresponding high-resolution DTM, but the inherent limitations must be considered in interpretation. Directional distortion due to map projection is minor for standard HiRISE images, which are reprojected in equirectangular projection with a center latitude near the image center.

We also documented the presence or absence of several possibly related geomorphic features in the vicinity of the scarps. These include scalloped depressions (*cf.* Morgenstern et al., 2007; Soare et al., 2008; Lefort et al., 2009; 2010; Zanetti et al., 2010), expanded craters (*cf.* Dundas et al., 2015; Viola et al., 2015), and irregular pits, all

306 of which may indicate sublimation and ice loss, as well as surface lineations indicative of
307 flow (*cf.* Squyres, 1978; Milliken et al., 2003). These features were documented if they
308 appeared on the same material unit as the scarp and were within 10–20 km distance. For
309 confirmed scarps with HiRISE coverage, we also documented smaller-scale features of
310 the scarp-hosting unit within hundreds of meters of the scarp crest. These included
311 polygons (interpreted as created by thermal contraction cracking; Mellon, 1997), surface
312 boulders, which are of interest since their occurrence on top of deposits potentially
313 originating as snowpack is surprising, and indications of layering exposed by the scarp,
314 which could preserve a climate record.
315
316 *2.3. Ice-Exposing Craters*
317 New impact locations are usually identified by manual searches of images from
318 CTX or other medium-resolution images, where they appear as dark markings due to
319 disturbance of surface dust (Malin et al., 2006; Daubar et al., 2013). This leads to a bias
320 towards detecting new impacts in high-albedo, low-thermal inertia (dusty) regions. These
321 detections are also dependent on having before-and-after imaging to constrain their
322 formation dates, and the availability of such imagery varies spatially and temporally.
323 Follow-up with higher-resolution imaging from HiRISE is usually needed to confirm the
324 presence of a crater and determine its size. In some cases at middle and high latitudes, the
325 new impacts reach deeply enough to excavate ice. The ice gradually sublimates, causing
326 excavated material to change color to match the nearby regolith over a period of months
327 to years (Dundas and Byrne, 2010; Dundas et al., 2014). Hence, only impacts formed
328 within the last few months or years are reliable probes for ice. Unfortunately, sublimation

329 and the associated fading of the ice exposures are fastest at the lowest latitudes, where the
330 presence or absence of ice is least certain, implying that detection of ice is also least
331 efficient at those latitudes. At higher latitudes, the seasonal polar cap is particularly
332 effective at obscuring fresh impacts, as dark blast zones within the bounds of the seasonal
333 cap are erased within the first winter (Dundas et al., 2014) due to dust deposition or
334 redistribution, although ice sometimes remains distinct. Additionally, the dark markings
335 surrounding new impacts can fade within several Mars years, and more changes to the
336 blast zones are seen at higher absolute latitudes (Daubar et al., 2016), likely due to
337 seasonal processes, implying that the overall detections of new craters are less efficient at
338 high latitudes.

339 A strong theoretical and observational basis indicates that shallow ground ice is
340 almost ubiquitous poleward of ~45–50 °N/S and rare equatorward of ~30–35 °N/S (e.g.,
341 Mellon et al., 2004; Bandfield and Feldman, 2008; Pathare et al., 2018; Piqueux et al.,
342 2019), but the true boundary within that range is an unknown that can be tested with
343 observations of these craters. Therefore, we examined all new craters poleward of 35
344 °N/S and made an interpretation of the icy status based on the criteria discussed below.
345 We use HiRISE enhanced color observations as our primary means of determining
346 whether ice is likely exposed. The ice exposed by craters is bright and generally appears
347 relatively blue or relatively white in HiRISE enhanced color. Relatively white coloration
348 is uncommon in non-polar HiRISE images and with appropriate context can be highly
349 indicative of frost or ice. Relatively blue coloration can also be due to mafic materials
350 (Fig. 3a), but we treat it as indicative of ice when other evidence is strongly supportive of
351 this interpretation: i.e., the material is substantially brighter than surroundings rather than

simply distinct in color. An additional indicator of ice is that material is distinct from other ejecta and crater floor materials, suggesting that some ejecta is ice and some is ice-free even if both are relatively blue. This is expected because the Martian surface is mostly mafic, even when ice is present. For small exposures, the ice is often in discrete patches with a distinct color relative to other excavated material. Other than the initial decision to only examine craters above 35°, latitude was not used to interpret the presence of ice, since the distribution of ice is not completely understood. Some material interpreted as ice was slightly relatively yellow, but substantially brighter than the surroundings and in settings where thermal contraction polygons also strongly support the presence of subsurface ice. Possible ice with a relatively yellow coloration has been reported in a gully alcove elsewhere on Mars (Khuller and Christensen, 2019), so this coloration is consistent with the presence of ice as well.

CRISM can provide definitive spectral tests for ice in some cases where the exposure is large enough (Byrne et al., 2009), but we do not use this as part of our diagnostic process because most of the marginal cases are small (2–10 m diameter craters) and unlikely to produce an unambiguous spectral signal in 18 m/pix CRISM data. In many cases appropriate CRISM observations do not exist. Three factors, however, support a general interpretation of the impact features meeting these color criteria as icy, rather than exposed salts or other bright lithic material: (1) CRISM confirmation of ice at several sites that share the indicators that we use for ice (Byrne et al., 2009); (2) lack of spectral detections of other materials that might account for the bright deposits; and (3) fading and disappearance over time consistent with sublimation at many of these sites (Dundas and Byrne, 2010; Dundas et al., 2014). Since there is a strong theoretical basis to

375 expect ice at these latitudes and cryogenic landforms are common around the craters, this
376 is the simplest interpretation; as discussed below, our diagnostic criteria are likely
377 underestimating the occurrence of ice.
378 We also note candidates where we consider the evidence for ice to be less
379 compelling. These are divided into (1) probable ice, where ice is our preferred
380 interpretation but not considered definitive due to very small size, weaker color contrast
381 with other ejecta, or lack of a well-defined crater; and (2) possible ice, where there is a
382 small color feature in the crater with minor contrast, or a bright feature that could be due
383 to topographic effects. Some sites initially classified as possible or probable were later
384 elevated to confirmed if the candidate exposure became less distinctive over time in a
385 manner consistent with sublimation and lag development (i.e., a color feature reverting to
386 match adjacent surfaces more quickly than the general fading of the blast zone).
387 Some low- and mid-latitude impacts (e.g., Fig. 3b) expose relatively bright
388 material that contrasts with a dark surface but is not interpreted as icy. Few of these exist
389 in our study latitudes. The surface geomorphology surrounding these sites generally does
390 not suggest ice (in particular, no polygons are interpreted as thermal contraction cracks).
391 Most of these craters occur at low latitudes (<35°) outside our survey area, where
392 theoretical models suggest that shallow ice is unlikely (e.g., Mellon et al., 2004).
393 Additionally, most or all of the ejected material is bright rather than isolated patches. At
394 low latitudes ice should be covered by a significant thickness (>1 m) of regolith or it
395 would otherwise sublimate rapidly, so if there were ice, it would occur in the ejecta as a
396 mix of ice and non-icy regolith. These bright ejecta deposits may be similar to exposures
397 of bright material by rover wheels in Gusev crater (e.g., Rice et al., 2011) or other

surface/subsurface compositional or grain size differences. While these craters provide information about the Martian subsurface, they are not considered further in this discussion of subsurface ice.

The icy craters that we document are those that expose persistent bright ice that remains distinct for months to years while sublimating, indicating clean ice with a low lithic content. Some apparently non-icy craters may have exposed subsurface pore ice, which would be all but impossible to detect from orbit. As shown by the Phoenix lander excavations, exposed pore-filling ice is dark, and in summer at mid-to-high latitudes it sublimates enough to create a surface coating that is indistinguishable from regolith within days (Mellon et al., 2009; Smith et al., 2009). This is much shorter than the typical time between the impact and acquisition of HiRISE images. Candidate impacts at high latitude are usually imaged by HiRISE within weeks of the initial detection in lower-resolution images, but that initial detection can be one to several years after the crater formed. One caveat is that the impact process may generate fractures and fine-grained material, which would be brighter than the pore ice exposed by the Phoenix lander, but a small amount of sublimation would still quickly produce an opaque cover under those conditions. Additionally, the small size of many of these craters means their shallow depths of only tens of centimeters may not be enough to reach the ice table. Finally, at high latitudes the seasonal cap reworks the surface, removing blast zones and obscuring ice, which can preclude detection and confirmation if craters are not imaged or re-imaged before winter. Thus, the set of craters we consider confirmed ice exposures are a minimum, and subsurface ice could exist at other known or unknown impact locations.

3. Scarp Observations

The full set of scarp exposures is given in Tables S1–S2 and mapped in Fig. 4. Below, we discuss some relevant morphological and geographical observations.

3.1 Scarp Distribution

In the southern hemisphere, 21 confirmed exposure sites were identified in the southern hemisphere (some with multiple scarps), along with two candidates lacking ice coloration, and one for which no HiRISE color data were available at the time of writing. The southern-hemisphere scarps are confined to a narrow range of longitudes near the Hellas basin, not evenly distributed throughout the latitude band. Most of the exposures are between 80–115 °E longitude and 50–61 °S latitude, similar to those previously known. A few occur in scalloped terrain (*cf.* Zanetti et al., 2010) at 50–61°E and a small cluster near 137 °E.

Scarps in the northern hemisphere are strongly concentrated in the mantling deposits within Milankovič crater (54.5 °N, 213.5 °E), which we subdivided into four sites in Table S1 based on the four cardinal directions. Over 70 features have the morphology of ice-exposing scarps at this location, although in HiRISE data some lack the relatively blue coloration indicative of exposed ice. Beyond Milankovič, a handful of scarp sites occur in crater-fill materials farther east, and one occurs in northern Utopia Planitia (96°E).

3.2 Scarp Morphology and Morphometry

Most scarps have a simple morphology (e.g., Fig. 1b), but a few have several subparallel faces (Fig. 5) or are divided into adjacent segments. Many exhibit faint, crude layering or color banding, but distinctive sub-meter-scale layers are uncommon (Fig. 6). Scarp lengths range from 200 m–6.5 km, and plan-view scarp widths range from 20–200 m. Length, width, and estimated retreat distance are loosely correlated (Fig. 7a, b). Latitude appears to weakly influence the upper envelope of scarp retreat distance, with somewhat greater scarp retreat at lower latitude (Fig. 7c). This may indicate active formation of new scarps, coupled with faster retreat at lower latitudes, because retreat distance should be a function of scarp age and sublimation rate. The latter will be influenced by latitude. However, the ratio of scarp length to retreat distance (the plan-view aspect ratio of the pits) shows no trend with latitude (Fig. 7d). This aspect ratio indicates the extent to which the scarp widens as it retreats. All scarps in both hemispheres approximately face the pole but most are oriented slightly east of due poleward, with a typical offset from N/S of 5–10°. This offset could relate to morning/afternoon asymmetries in temperature combined with the thermal inertia of the surface reducing peak temperature. Individual scarps have along-scarp orientation variations on the same order as this offset.

The one scarp for which high-resolution topographic data exist (southern scarp #1) has typical slopes of ~45° with moderate variations both vertically and laterally (Dundas et al., 2018). Shadow-derived estimates at four locations on this scarp are 47–49°, demonstrating that the method gives reasonable results for typical scarp geometry. Shadow-derived slope estimates for other scarps with appropriate shadow conditions are given in Table S3. In the southern hemisphere, slopes range from 41–60°, with most

between 45–50°. In the north, a variety of confirmed and candidate exposures have slopes of 40–64°. The mean slope in the north (53°) is similar to that in the south (49°). These estimates suggest that southern scarp #1 is typical. These slopes indicate that the plan-view widths of the scarps approximate the vertical relief to within a factor of 2. Furthermore, the pits do not necessarily reach all the way to the bottom of the ice, so the ice thicknesses may be even larger.

As reported in Dundas et al. (2018), scarp-parallel features indicate that scarps retreat generally equatorward and that retreat is uniform along the length of the scarp. Triangular or other shapes of the resulting pits indicate that the scarp width can vary over time (Fig. 8). Scarp retreat appears to be close to uniform along the length of the scarp, such that when the retreat direction is oblique rather than normal to the scarp, the orientation of the scarp remains unchanged (Fig. 8). Notches in the plan-view shape of pits (Fig. 8) suggest that scarp retreat occasionally reactivates only over part of its length; the other parts may reactivate later, giving rise to the small parallel outliers seen in some pits. The aspect ratio of the scarp pits shows substantial scatter (Fig. 7d), so the rate at which scarps widen as they retreat is highly variable.

3.3 Scarp Setting

The regional properties of the locations are broadly similar in both hemispheres. All of the identified scarps occur within deposits that appear to mantle the regional surface (Fig. 9); although in a few cases, the uppermost part of the mantling deposit may have been removed (Fig. 9c). In the southern hemisphere, the kilometer-scale regional slopes around the scarps and pits are mostly pole-facing but generally low (typically ~5°

489 in the Mars Orbiter Laser Altimeter digital elevation model), and some are nearly flat.
490 The scarps there are often associated with the slopes of few kilometer-scale local massifs
491 or crater walls. In the northern hemisphere, the vast majority of scarps and candidate
492 scarps are in Milankovič crater. They are found on all slope orientations therein, but
493 primarily on the west side of the crater (Fig. 10). As in the south, the regional slopes are
494 generally low. The material on the slopes of the crater may have a low density (at least
495 within the upper 5 meters) as it has a low radar surface reflectivity (Morgan et al., 2020).
496 The other northern-hemisphere candidates are found within materials that infill few
497 kilometer-scale impact craters. The regional albedos from the Thermal Emission
498 Spectrometer (TES; Christensen et al., 2001) are all close to 0.2, and the regional
499 apparent thermal inertias from TES (Putzig and Mellon, 2007) are between 128–225 J m^{-2}
500 K^{-1} $s^{-0.5}$, consistent with a surface layer of unconsolidated dry soil a centimeter or more
501 deep, with the sole exception of the site in Utopia.
502 Although the scarps are characteristically within mantling deposits, the associated
503 geomorphology is variable. Candidate ice-loss features (scalloped depressions and
504 expanded craters) are found near some of the scarps, but in most cases the landforms are
505 not well-defined examples. However, irregular pits that do not closely match the
506 scalloped or expanded morphologies are almost ubiquitous across the scarp-hosting
507 mantling deposits. Arcuate lineations indicative of ice flow are uncommon. In the plateau
508 material at the top of the scarp, polygons (likely due to thermal contraction of ice) are
509 common but not ubiquitous, and often not well defined, which may indicate that the ice is
510 deep enough to not experience strong thermal cycles or that it anneals effectively without
511 infall of material into the cracks. In some cases the surface material consists of aeolian

512 bedforms and so may currently be too mobile to develop defined polygons. The brink of
513 the scarp is often broken into blocky fragments that might be defined by subtle polygonal
514 fractures that have generated little surface relief. Polygons are also common on the walls
515 and floors of some pits. The upper surface of the scarp-forming material usually has few
516 boulders, particularly in the northern hemisphere.
517 CRISM data confirm exposed ice at several scarps (Table S1) beyond those
518 described in Dundas et al. (2018). Detections at two of the scarps were independently
519 confirmed by Harish et al. (2020). Notably, one observation of the icy scarp at 57 °N,
520 95.7 °E (northern scarp site #4) shows a distinct water ice signature, as well as an
521 ambiguous spectral signature in the visible to near-infrared, suggesting impure ice. The
522 simultaneously acquired HiRISE image shows only a weak color signature covering parts
523 of the scarp, leading to a classification of confirmed but marginal. This suggests that all
524 scarps with the classic morphology could be ice exposures, regardless of coloration.
525 Either the covering lag is too thin to completely suppress the ice spectral signature or the
526 lithic content of the ice is high enough in some cases that the coloration seen in HiRISE
527 is minimal. If the coloration is from a lag coating, it must be very thin, as a dust coating
528 of tens of microns can be opaque at visible wavelengths (Wells et al., 1984; Fischer and
529 Pieters, 1993). If the coloration reflects the bulk ice composition, this is still consistent
530 with a high ice content. Cull et al. (2010) show that for as little as 10 weight % lithics
531 (>95 volume % ice) the visible color contrast may be minimal, and Clark and Lucey
532 (1984) showed substantial darkening and weak spectral absorption features for even
533 smaller amounts of non-ice material, depending on its albedo. Further monitoring with
534 HiRISE might distinguish between these possibilities, as lags could be removed

episodically. Harish et al. (2020) also noted some scarps at northern scarp site #5 with relatively blue coloration but no spectral signature of ice, likely because the scarps were substantially shadowed.

Numerous pits were examined and determined not to meet the morphological criteria for likely ice exposures. Some of these may be former scarps that have become buried under sublimation lags that are thick enough to obscure the sharp morphology of clean exposures. Examples of pits without distinct scarps are shown in Fig. 11 for comparison, and Fig. 8 shows a pit that mostly lacks exposures apart from a small outlier scarp.

4. Crater Observations

HiRISE images now cover 48 ice-exposing impact sites (Fig. 12 and Table S4). The diameter of ice-exposing and non-ice-exposing craters poleward of 35 °N/S is shown in Fig. 13. Diameter scales linearly with maximum excavation depth for small craters (Melosh, 1989), and Fig. 13 also shows 0.084× the crater diameter. This value is given since the maximum excavation depth is ~1/10 of the transient crater diameter and the transient crater is ~0.84× the final diameter for simple craters (Melosh, 1989); although seemingly precise, this depth should only be treated as an approximation. The data set is more extensive than that in Dundas et al. (2014) but is broadly similar and does not change the interpretations made therein. Those include the widespread occurrence of clean ice with local heterogeneity, as well as the latitudinal distribution in the northern hemisphere, which suggests that the long-term atmospheric water vapor content was higher than at present and/or that there is a near-surface concentration of vapor. The

morphology of the ice exposures ranges from small fractions of the crater interior to extensive icy ejecta. Several important new observations and their interpretations are discussed below.

Weak material over a strong layer produces characteristic crater morphologies of flat floors and benches or terraces for craters with diameters approximately 4–10 times the weak layer thickness (Quaide and Oberbeck, 1968). The depth to the strong layer can be estimated using the methods of Bart (2014). For sites with exposed ice, there is a high likelihood that such a strong layer is the top of the ice table since the ice is known to exist and should provide a strength contrast. We apply this method at sites with multiple flat-floored craters. Those craters are often not the same as those with visible ice, since the ice exposures tend to be in the largest craters that penetrate more deeply into the ice table. (For sites without confirmed bright ice, the morphology could be produced by pore ice but also by shallow bedrock or another strength contrast, making the interpretation less certain.) The results (Table 1) show significant variability in depth to the strong layer between different craters in individual clusters. This likely reflects both real local depth variation and measurement uncertainty. In combination with differences in the visibility of ice in similarly sized craters (Dundas et al., 2014), this indicates that heterogeneities in the ice table depth and ice content are significant at scales of tens to hundreds of meters.

Fewer new craters (icy or not) have been discovered in the southern hemisphere in comparison with the north, mainly because the less extensive dust cover in the south inhibits detection, but also due to different imaging and search techniques that vary by region. The distribution is still sufficiently sparse that the southern latitudinal boundary is not well defined. However, the number and distribution of icy impacts observed in the

581 southern hemisphere has expanded significantly relative to Dundas et al. (2014), and the
582 lowest-latitude ice detection in the south is now at 46.2 °S. That crater is on a slight pole-
583 facing slope with nearby gullies and thus may not be representative of level ground, but
584 there is also a probable candidate on flat ground at 42.6 °S.

585 In the northern hemisphere, the lowest-latitude detection remains at 39.1 °N. This
586 location is part of a southward excursion of icy crater detections extending between
587 ~145–205 °E where ice detections are common between 40–50 °N (Fig. 12). This
588 contrasts with a lack of confirmed icy craters at those latitudes between 205–255 °E. The
589 region lacking icy craters corresponds to terrain where stability models predict that ice
590 should be quite shallow and extend particularly far towards the equator due to high
591 albedo and low thermal inertia (Mellon et al., 2004), so it is possible that pore ice is
592 dominant at the top of the ice table there. Some of the non-ice-exposing craters in this
593 area have flat floors which could indicate such a pore ice table, but this interpretation is
594 nonunique. At other longitudes, new crater detections between 40–50°N are sparse, and
595 the only other ice detections equatorward of 47.4 °N are on lineated valley fill; these
596 detections may not indicate extant ice under the surface in those areas apart from within
597 the lineated valley fill.

598 Two craters near Protonilus Mensae excavated lineated valley fill and confirm the
599 presence of ice within a few meters of the surface there between 41–42 °N (Fig. 14). This
600 could be the top of glacial ice that has been detected in similar material by the Shallow
601 Radar (SHARAD; Holt et al., 2008; Plaut et al., 2009; Petersen et al., 2018), the top of
602 which is not detectable at SHARAD resolution (approximately 10 m in ice); however,
603 ice-rich lenses or other structures within a thicker debris cover cannot be ruled out. In the

604 eastern part of the crater shown in Fig. 14a, ice exposed in the crater wall appears to
605 make up the core of a surficial topographic ridge (a part of the surface type sometimes
606 referred to as “brain-coral” or “brain” terrain (e.g., Noe Dobrea et al., 2007; Levy et al.,
607 2009b)) that was cut by the impact, providing information about the subsurface structure
608 of such material. In both of these craters the visible ice exists mostly in discrete blocks, in
609 contrast with most others; this suggests that the shallow subsurface ice is in discrete
610 bodies surrounded or covered by ice-free debris, which may indicate that ice at these
611 locations is unstable and sublimating, since ice would be expected to cement the regolith
612 pore space at these depths if it were stable.

613 Polygons attributed to thermal contraction cracking (e.g., Mellon, 1997) are
614 nearly ubiquitous at the sites of ice-exposing impacts. They are occasionally found
615 around new impacts where HiRISE images do not show bright ice but much less
616 frequently. At some of those sites impacts probably exposed pore ice or did not excavate
617 to the depth of the ice table. This suggests that thermal-contraction polygons and present-
618 day ice are strongly correlated and that relict ice-free polygons are uncommon. However,
619 the morphology of the polygons is diverse, including high-centered and low-relief
620 features, irregular or incomplete polygon networks, as well as regularly spaced low-relief
621 hummocks without defined fractures. Thus, the relationship between the detailed polygon
622 morphology observable at HiRISE resolution and the presence of excess ice is not simple,
623 but ice-exposing craters are sparse and offer limited information about the vertical
624 structure of the ice.

625 An 18 m-diameter crater that formed on the south polar layered deposits (SPLD)
626 during southern winter of Mars Year 34 showed minimal bright ice once the seasonal

627 frost had vanished (Fig. 15ab) and was classified as probable. This crater is discussed
628 more extensively in Landis et al. (2020). A second crater cluster in the southern mid-
629 latitudes has been observed to form with ejecta superposing seasonal frost (Fig. 15c).
630 This site also lacks bright ice once defrosted, but the craters are much smaller and may
631 not have excavated to ice. In both cases the crater morphologies appear minimally
632 affected by the presence of CO_2 frost at the time of impact, demonstrating that seasonal
633 frost probably has little effect on the long-term cratering record except for extremely
634 small craters.

635 The SPLD and Protonilus craters also enable us to assess whether any of the
636 observed bright ice is due to melting/refreezing (*cf.* Reufer et al., 2010) or condensation
637 of vapor post-impact, rather than representing the original state of ground ice. If the
638 former were the case those effects would be expected to be strongest in the largest
639 craters, which represent the most energetic impacts. Small bolides should be slowed by
640 the atmosphere and their small craters should have little if any melting, so we can rule out
641 the possibility of impact generation of clean ice if it does not occur in the larger craters.
642 The 18 m crater on the SPLD (Fig. 15a, 15b) is larger than most lower-latitude craters
643 with visible ice exposures but has negligible amounts of bright ice. The SPLD certainly
644 contains significant ice content in bulk (at least 85%; Plaut et al., 2007; Zuber et al.,
645 2007) although the near surface could be pore-filling ice, and theory indicates that ice
646 should begin at depths of centimeters there (e.g., Mellon et al., 2004). Likewise, discrete
647 ice blocks occur around the largest ice-exposing crater (Fig. 14a) as well as several
648 others. Long-baseline temporal monitoring of several craters demonstrates shrinking and
649 disappearance of blocks of ejected ice, as reported at other sites by Dundas et al. (2014),

suggesting that the blocks are massive ice. These blocks are inconsistent with melt pools or condensation. Thus, several of the largest ice-exposing craters have characteristics that show that the bright ice is not produced by the impact process. This implies that the observed clean ice represents the natural state of the pre-impact ice for most or all craters. High ice contents (well above pore-filling) are widespread in the shallow subsurface at latitudes above ~40 °N.

Only five of the confirmed ice-exposing impacts have an H_2O ice signature in CRISM data (Table S4), while 23 have CRISM data without an ice detection. All five are among the larger craters or clusters of several craters and have large swaths of ice in their ejecta rather than small exposures in the crater itself. In some locations, we also analyzed repeat CRISM observations, but the absorption bands attributed to water ice were weak and barely detectable above the noise. Either atmospheric haze, accumulated surface dust, or spectral mixing and signal being averaged into multiple pixels precluded detection of ice in the later CRISM images after the initial observation. This demonstrates that extensive areal exposures and contemporaneous observations are required for ice detection by CRISM, as even the largest ice exposures only occupy portions of a handful of pixels.

5. Discussion

5.1. Importance of Subsurface Ice Exposures

These surveys of scarps and craters directly provide information about the nature and distribution of subsurface ice on Mars. They also provide an extensive set of locations that can be used for validation of the presence and properties of ice indicated by

673 other data and models. While they have not been studied in situ, these locations provide
674 more direct and localized information on the state of the ice than other methods currently
675 available. This level of verification and detail is useful for interpreting other data sets
676 (e.g., Pathare et al., 2018; Piqueux, et al., 2019), for design of possible ice-detection
677 instruments (e.g., Haltigin et al., 2018), and for the possible use of ice by human
678 explorers (*cf.* Heldmann et al., 2014; Putzig et al., 2020).
679 Both the craters and scarps provide information about the local state of the ice
680 table, but the difference in the nature of the exposure and exposure process poses
681 challenges for analyzing the two together. For instance, impact-exposed ice is often
682 relatively white while the scarps are generally relatively blue. This may indicate some
683 degree of impact modification (e.g., fracturing reducing the grain size or increasing
684 porosity). Additionally, these differences in relative color could in part be related to the
685 surrounding terrain. Quantitative photometry including assessment of topography and
686 atmospheric scattering is needed before such color differences can be confidently
687 interpreted. The craters represent semi-random samples (subject to detection biases),
688 while certain regions or certain ice properties may be conducive to scarp formation, as
689 discussed below. Finally, different properties are measurable for each: for instance,
690 craters primarily provide information on the depth to ice. Scarps place lower bounds on
691 the ice thickness, but the depth to the top of the ice may be obscured by material falling
692 from the scarp crest. Despite this, in some places ice, can be seen within 1 m of the scarp
693 crest (Dundas et al., 2018) and could be exposed by craters.
694 The expanded surveys presented here are generally consistent with previous
695 interpretations of the state and distribution of ice based on a more limited sampling of

features (Dundas et al., 2014; 2018). The larger data sets presented here do provide several new insights into the origins, properties, and distribution of subsurface ice, discussed in the following sections.

5.2. Distribution, Properties, and Origins of Subsurface Ice

The lowest-latitude detection of ice based on craters is unchanged in the north compared with Dundas et al. (2014). Exposure of clean ice by new impacts is common, indicating that such ice is widespread at shallow depths. The poleward-shallowing trend of ice in crater exposures reported by Dundas et al. (2014) is confirmed by the additional data reported here, with depth and latitudinal boundary similar to theoretical predictions. Poleward of ~50 °N/S latitude, most dated new impacts either definitely or possibly expose bright ice. In crater clusters the larger craters generally expose bright ice and the smaller ones do not (Table S4), but in several instances this relation is reversed. The latter requires lateral heterogeneities in the distribution or concentration of ice in the upper meter of the subsurface or variable impact properties and distribution of ejecta. The depth to ice also has significant local variability when measured within crater clusters (Table 1), consistent with theoretical predictions (Sizemore and Mellon, 2006) and excavations by the Phoenix lander (Mellon et al., 2009).

The apparent variation in icy crater detections between 40–50 °N, from frequent icy craters between 145–205 °E to a lack at 205–255 °E, corresponds with features in several other data sets. This zone of low-latitude icy craters corresponds to a region where neutron spectroscopy shows high ice content (greater than pore-filling) extending to lower latitudes than in the rest of the northern hemisphere (Pathare et al., 2018). The

719 transition near 205 °E approximately matches the transition from abundant expanded
720 craters (to the west) to few (to the east) in the mapping of Viola et al. (2015), although
721 that map has little coverage west of 190 °E. Viola and McEwen (2018) show that
722 expanded craters equatorward of 40 °N are concentrated between 185–205 °E. The zone
723 of icy craters also corresponds to radar detections of a low dielectric constant (interpreted
724 as indicating a high ice content extending to tens of meters depth), which are
725 concentrated between 180–215 °E (Bramson et al., 2015) and interpreted as a regional ice
726 sheet. The high bulk ice content of this unit has been challenged based on radar loss
727 tangent estimates (Campbell and Morgan, 2018), but the agreement of the ice exposures
728 and neutron spectroscopy suggests that at least the upper centimeters of the material are
729 ice-rich, which is further supported by the observation of expanded craters (Dundas et al.,
730 2015).

731 A similar ice sheet has been proposed in the Utopia region (Stuurman et al., 2016)
732 based on mapping of radar reflectors that indicated a dielectric constant similar to that of
733 ice. No new impact detections are in the region of radar reflectors mapped by Stuurman
734 et al. (2016), likely because a lack of surface dust makes such detections rare (Fig. 12).
735 However, one ice-exposing crater is within the broader geomorphic unit of mesas and
736 scalloped depressions (Kerrigan, 2013) that contains the reflectors. Such scalloped
737 depressions have been attributed to partial sublimation of an ice-rich unit (e.g.,
738 Morgenstern et al., 2007; Lefort et al., 2009; Zanetti et al., 2010; Dundas et al., 2015), the
739 top of which may be indicated by the crater exposure.

740 Scarp exposures provide relatively weak constraints on the global distribution and
741 properties of ice on Mars, since they are at higher latitudes than many of the craters and

742 may not reflect the typical state of shallow subsurface ice. However, they provide
743 important constraints on local properties. The scarps generally occur in surface-mantling
744 deposits. Mantling deposits that have been interpreted as ice-rich are common at middle
745 to high latitudes (e.g., Mustard et al., 2001; Head et al., 2003; Milliken et al., 2003;
746 Schon et al., 2009); the scarp regions appear somewhat more extensively mantled than
747 other areas, but this is difficult to quantify. The fact that scarps occur only in a narrow
748 latitude band in both hemispheres suggests that some process controlled by latitude is
749 important to exposing the ice, meaning that similar ice could exist elsewhere. However,
750 since the scarps are concentrated at certain longitudes while ground ice is expected to be
751 ubiquitous at these latitudes (e.g., Mellon et al., 2004; Schorghofer and Aharonson, 2005;
752 Chamberlain and Boynton, 2007), some other factor(s) relating to the state of ice or the
753 physical processes exposing it is also necessary to explain the scarp distribution. These
754 observations can be explained if ice exposures occur within a subset of mantling deposits
755 where ice is particularly thick and/or pure, providing longitudinal or local control, and if
756 particular latitudinal conditions (e.g., insolation and temperature) are required to create
757 and maintain the exposure. Supporting this possibility, the scarps in the southern
758 hemisphere are mostly located in longitudes where neutron spectrometer data show high
759 ice contents (60–90 weight percent) extending to relatively low latitudes (Pathare et al.,
760 2018). The same region also overlaps the location of the largest concentration of
761 scalloped depressions and thermokarst landforms in the southern hemisphere (Zanetti et
762 al., 2010; Viola and McEwen, 2018), also consistent with high ice contents. Scarps and
763 their host mantling units often appear localized near massifs or crater walls, which might
764 help concentrate snow deposition in incipient glaciers, but these correlations with other

765 data sets suggest that the scarp-hosting ice bodies are associated with high regional ice
766 contents. In this interpretation, the ice at the exposures represents an ice-rich end-member
767 of the diversity of Martian near-surface mantling and ice deposits. Fully testing this
768 hypothesis requires more information on the state of ground ice at locations without
769 scarps; crater exposures are too shallow to provide a full comparison.
770 The ice exposed in the scarps likely originated as snow or frost, which has now
771 been compacted. This is based on two main lines of evidence. First, the hosting units
772 typically drape the surface in a manner consistent with atmospheric deposition rather than
773 infilling topographic lows, and the scarp properties imply a very low lithic content
774 (Dundas et al., 2018). Second, the fine crosscutting layers observed at some scarps (Fig.
775 6) are most consistent with snow, since subsurface growth of ice lenses or other
776 structures (e.g., Sizemore et al., 2015) would likely parallel the surface and not produce
777 crosscutting relationships. (This could arise within an airfall deposit that was partially
778 eroded and then covered, but the high ice content (Dundas et al., 2018) is better explained
779 by snow or frost.) Moreover, non-snow theories for the development of high subsurface
780 ice contents on Mars, such as ice lens growth or enhanced vapor diffusion (e.g., Fisher,
781 2005; Sizemore et al., 2015) operate in the near surface rather than building units >100 m
782 thick.
783 The presence of boulders on the surface of scarp-hosting units was noted as a
784 puzzle by Dundas et al. (2018). If the massive ice deposits are consolidated snow, they
785 should lack clasts larger than windblown sand or dust. The additional scarps included in
786 this larger sample set mostly exhibit few or no surface boulders at the top of the unit. This
787 observation is more favorable for a snowpack model than are abundant boulders, but the

788 presence of any large rocks remains a puzzle. Rocks can be concentrated by sublimation
789 processes (Aylward et al., 2019), but must be present initially. Indications of glacial-style
790 flow are rare at these locations, so rafting to concentrate rocks at the surface may be an
791 insufficient explanation for boulders superposing the ice. An alternative is that boulders
792 are lifted and held at the surface during ice accumulation (Schorghofer and Forget, 2012),
793 but boulders are embedded within ice at one scarp (Dundas et al., 2018). A similar
794 process of locking boulders within seasonal CO_2 frost and moving them via differential
795 thermal contraction is a possible explanation for horizontal boulder sorting at other
796 locations (Orloff et al., 2013). An additional possibility is that these surface boulders are
797 ejecta from nearby impact craters, although the sparse craters on the surface of the
798 mantling deposits suggest that impacts since those deposits were emplaced were not
799 sufficient. The scarps surveyed here are distinctly different from the steep slopes at the
800 edge of the north polar layered deposits (NPLD), which have slopes up to 70° over 300-
801 meter baselines and are approximately vertical over some shorter intervals (Russell et al.,
802 2008). These slopes also occur in a body of ice with low dust content, estimated to be
803 <2% (Picardi et al., 2005). Despite active avalanching and slope retreat (Russell et al.,
804 2008), the NPLD scarps generally have dusty coloration except on the flat residual cap
805 (Byrne, 2009), although because this is inferred from relative color, quantitative
806 inferences about the ice content are difficult.
807 In comparison with the scarps, the craters provide relatively little constraint on the
808 deposition and modification processes of the ice. They demonstrate the widespread
809 occurrence of processes that create high ice contents in the shallow subsurface, but the
810 small penetration depth and exposure size, and disruption of the ice by impact, make it

811 difficult to distinguish between the various candidate processes. Boulders are common
812 around many of the craters, as at the scarps.
813
814 *5.3. Scarp Formation and Evolution*
815 The scarps pose a significant puzzle: how is the bare ice exposure created and
816 maintained, when a covering lag is expected to develop within years and sublimation is
817 actively occurring? Landscape evolution modeling suggests that a steep exposure of
818 dusty ice would gradually become shallower because the base would be buried under the
819 debris released by its own sublimation and retreat (Dundas et al., 2015). The straight
820 geometry of the scarps may reduce this effect because the debris at the base is not
821 collected from a wide area. The scarps are quite steep and could shed debris rather than
822 accumulating a surface cover, like the steep slopes of parts of the NPLD (Russell et al.,
823 2008). This appears to be occurring in some cases, but in at least one example the process
824 is building a debris-covered lower slope and deactivating sublimation on the lower scarp
825 (Dundas et al., 2018). Some scarps may be partially or completely debris covered (Figs.
826 2b, 8, 11), so in some conditions this process may cease. Additionally, how such a slope
827 is created in the first place or how scarps reactivate after accumulating surface debris is
828 not obvious. The scarps do not resemble impact features, which are typically circular, but
829 runaway growth from small impacts is a possibility. Fault movement can be ruled out at
830 one location by a lack of vertical offset (Dundas et al., 2018), and at no site is there any
831 indication of fault-like deformation extending beyond the scarp. Additionally, ridges
832 indicating scarp retreat are inconsistent with movement on a fault. The scarps face the

833 pole regardless of the slope orientation and sometimes occur on level surfaces, which
834 rules out any gravity-driven failure.
835 Two possible factors in creating and maintaining scarps are seasonal frost and
836 aeolian transport. CO_2 frost can transport material either via basal sublimation (e.g.,
837 Kieffer, 2007; Pilorget and Forget, 2016) or by loading a steep slope and avalanching as
838 observed at the NPLD (Russell et al., 2008), and winds could also strip away a
839 sublimation lag. The gradual fading of color contrast and weakening of ice spectral
840 signatures on one scarp over the course of a summer (Dundas et al., 2018) were
841 consistent with frost effects, as a lag might accumulate over the summer before being
842 removed by frost in the following winter and spring, and lineations suggesting frost-
843 driven mass wasting occur on scarps in early spring images (Fig. 16a). The latitudinal
844 dependence of scarp occurrence is consistent with a role for CO_2 frost but would require
845 some additional control, since such frost is ubiquitous in the winter at middle and high
846 latitudes, and the abundance on the scarps is not known. Frost and wind effects are not
847 mutually exclusive. Ridge structures at some scarp locations (Fig. 16b) resemble features
848 interpreted as dust bedforms (Geissler, 2014) or indurated dust (Bridges et al., 2010)
849 elsewhere on Mars. These are oblique to the scarp and cut by it, suggesting limited
850 mobility relative to the scarp retreat timescale. For comparison, modeling of sublimation
851 conditions at migrating NPLD trough sites suggests that removal of a sublimation lag by
852 surface winds is likely necessary for sublimation to continue over prolonged periods there
853 (Bramson et al., 2019).
854 Cliffs on terrestrial debris-covered glaciers offer both insights and contrasts. Cliff
855 exposures can be created by sliding of the debris layer, or collapse into lakes or meltwater

conduits (e.g., Kirkbride, 1993; Sakai et al., 2002). Neither of these is likely on Mars, given the low slopes and lack of a significant meltwater system at Martian temperatures. In the Himalayas on Earth, equator-facing slopes are quickly covered by debris, while pole-facing ice cliffs persist and act as important drivers of ice loss, because they receive less insolation and are steep enough to shed debris (Sakai et al., 2002; Buri and Pellicciotti, 2018). Differences in the radiative balance of the upper and lower parts of the slope as a function of aspect are important to the development of the cliffs: at some aspects, melting and retreat of the lower slope is enhanced, helping to maintain a steep exposure, while for others the reverse is true (Sakai et al., 2002). If such a dependency exists for the relevant conditions on Mars, then for sufficiently clean ice, it could enable steepening and runaway growth of a small exposure. A somewhat similar process is observed in models of scalloped depressions, where small disturbances initially cause the bottom of a depression to drop rapidly (Dundas et al., 2015). Antarctic analogs indicate that calving of blocks via thermal expansion-induced cracking may be an important driver of the retreat of steep scarps (e.g., Levy et al., 2013). This has not yet been observed on Mars but is possible, and the scarp faces often appear fractured.

In a number of cases, scarps occur in the vicinity of other possible ice-loss landforms and sometimes definitively within the same unit (e.g., Fig. 9). The relationship between the scarp pits and scalloped depressions (e.g., Morgenstern et al., 2007; Soare et al., 2008; Lefort et al., 2009; 2010; Zanetti et al., 2010) is not fully understood, but they appear to form and evolve differently. The major evidence for this difference is that linear ridges are observed parallel to some scarps (Fig. 8), indicating that the scarps retreat in a straight line. Scalloped depressions, by contrast, have arcuate internal ridges

(Lefort et al., 2009; Dundas, 2017a). The scarps typically widen as they retreat, resulting in crudely triangular pits that are narrow on the poleward side and widest at the exposed scarp, unlike scalloped depressions (Fig. 9c) and suggesting localized origination. Additionally, the largest scarp pits are commonly multiple kilometers across and occur in relative isolation, while scalloped depressions are typically smaller until mergers create larger complex landforms. Scalloped depressions are commonly interpreted to be sublimation-thermokarst that form via sublimation of an ice-rich unit much like that revealed in the scarps (Morgenstern et al., 2007; Lefort et al., 2009; 2010; Zanetti et al., 2010; Dundas et al., 2015), so one possibility is that they represent different styles of evolution relating to the occurrence of exposed surface ice versus loss through a lag. Poorly defined expanded craters also occur near some scarps. These are interpreted as sublimation-modified impact craters (Dundas et al., 2015; Viola et al., 2015), and the best examples are in Milankovič crater (Fig. 9b). However, while the expanded craters there appear in surface-mantling deposits similar to those hosting the scarps, they are generally not adjacent: the expanded craters are mostly outside the rim of Milankovič, while the scarps are in the crater interior. This could indicate a difference in material properties or surface age, since most of the expanded craters in this region of Mars may be tens of millions of years-old secondary craters (Viola et al., 2015), so the surface-mantling deposits within the crater could be younger. Alternatively, this could indicate a role for the effects of local slope or topography. Near the scarps, irregular pits are more common than either scalloped depressions or expanded craters; given the setting and substrate, these probably also represent ice-loss features.

Rather than treating scarps, scalloped depressions, and expanded craters as entirely distinct features, they may be best viewed as the result of different initial conditions and evolutionary pathways for ice-rich deposits affected by sublimation, frost, and wind. Hence, scallop-like landforms arise when disturbances destabilize the surface and cause sublimation through a lag, and expanded craters are fundamentally similar but result from relatively large initial disturbances (impacts) that are not completely erased by sublimation as the crater expands. In cases of strong sublimation, expansion might eventually make the original crater unrecognizable and transition to a scallop-like feature. Both of these morphologies have been effectively modeled via lag-controlled sublimation alone (Dundas et al., 2015; Dundas, 2017a) and retreat should concentrate on the warmest, least-stable slopes. Exposed scarps fit within this framework if they represent a different mode where wind, CO_2 frost, or other factors maintain a bare ice surface which retreats more quickly than ice that is covered by lithic debris, and thus occurs on the slopes where those effects are strongest. The typically straight scarp morphology represents a notable contrast from the other features. Individual landforms could change modes: for instance, a scarp exposure might emerge within a scalloped depression if erosion on the pole-facing slope removes lithic debris, and scarps could become buried if the debris ceases to be removed effectively. The resulting morphologies could be compound features dependent on the initial conditions and variations of the driving forces over time, due both to climate variations and the changing shape of the landform itself. This model raises two important questions. First, under what circumstances do these processes produce well-defined scalloped depressions or expanded craters versus irregular pits? And second, in regions of unstable or marginally stable ice, how much ice

924 is lost to the atmosphere by this localized landform evolution, in comparison with
925 uniform sublimation?
926
927 *5.4. Implications for Martian Climate and Ice Processes*
928 The present-day distribution and properties of ice on Mars record the history of
929 climate, as they reflect an integrated history of deposition, internal processes (such as
930 densification and ice-lens formation), and sublimation. Ice that exists today is either
931 aggrading, stable, or was originally deposited in such abundance that subsequent periods
932 of instability have not been sufficient to remove it. The observations and interpretations
933 above provide some high-level insights about this history.
934 Atmospheric water vapor content is a major control on the distribution of stable
935 ice. If the ice-exposing craters are sampling the upper part of a thick massive ice body in
936 the Arcadia region as discussed above, then the elevated atmospheric water content
937 required to stabilize ice at the lowest-latitude craters (Dundas et al., 2014) might date to
938 the time of deposition or a time-integrated average over subsequent time rather than the
939 most recent climate, since thick ice units can survive over protracted periods while slowly
940 sublimating (e.g., Schorghofer and Forget, 2012; Bramson et al., 2017). If the ice was
941 deposited as snow, that water content would be a lower bound, since surface snow
942 deposition requires more water vapor than subsurface stability. However, the lag
943 developed during retreat must be thinner than predicted by Bramson et al. (2017)
944 assuming nominal conditions for the present day, or the shallow subsurface ice probed by
945 these craters contains excess ice above the deposit indicated by the radar reflectors.
946 Alternative histories for atmospheric water vapor might allow survival with a thinner lag,

947 or sublimation lags may restrict sublimation more than observed in laboratory
948 experiments (Hudson et al., 2007). A generalized latitudinal model by Schorghofer and
949 Forget (2012) does allow lags <1 meter over ice sheets with ages of a few million years
950 or less. The survival time of such ice sheets depends on both the climate history and the
951 time and amount of deposition, as well as the thermophysical properties of the lag itself.
952 As discussed above, scarps may indicate locations of particularly thick, clean ice
953 deposits originating as snow. The apparent high ice content at the scarps suggests that the
954 ratio of ice to dust in the atmosphere was high when deposition was occurring at those
955 locations. Scarps might not exist in all such deposits, and the specific ice bodies hosting
956 scarps may be influenced by local topography. Nevertheless, the scarps likely indicate a
957 subset of favored locations for past ice deposition. Several general circulation model
958 (GCM) studies have examined potential locations of past tropical or mid-latitude snow or
959 frost accumulation under different orbital configurations and axial tilt, with significant
960 differences in the details of model physics as well as in assumptions about H_2O sources
961 and atmospheric dust abundance (e.g., Levrard et al., 2004; Forget et al, 2006; Madeleine
962 et al., 2009; 2014). Due to these differences and the limited sweep of parameter space
963 with any individual model, stating a simple hypothesis that could be tested by comparison
964 with the scarp distribution is not possible at present. Several scenarios do produce
965 concentrated ice accumulation south and southeast of the Hellas basin (hereafter SSE
966 Hellas), which has a marked influence on atmospheric circulation. These include
967 scenarios with low obliquity (15–25°) and an equatorial ice source, particularly with a
968 high optical depth of dust in the atmosphere (Levrard et al., 2004; Madeleine et al.,
969 2009), but also scenarios with 35° obliquity and no equatorial ice source (Madeleine et

al., 2014). The seasonal timing of perihelion also strongly affects deposition patterns (Madeleine et al., 2009; 2014). Forget et al. (2006) produced strong deposition east of Hellas, equatorward of the scarps, in a model scenario with 45° obliquity and surface ice at the south polar cap. Scenarios with both low and high obliquity can also produce deposition in the region near Milankovič crater (Madeleine et al., 2009). Other locations of predicted ice deposition in various scenarios do not correspond with scarps, although some match the locations of debris-covered glaciers (e.g., Holt et al., 2008; Plaut et al., 2009; Levy et al., 2014), scalloped depressions (e.g. Morgenstern et al., 2007; Lefort et al., 2009; 2010; Zanetti et al., 2010), or expanded craters (e.g. Viola et al., 2015). The evidence from the scarps favors the past occurrence of one or more of the climate scenarios that produce strong deposition at the scarp locations, and the low dust content of the scarp ice may favor those that produce accumulation with a low optical depth atmosphere. However, Mars' orbital elements have varied widely (e.g., Laskar et al., 2004) and the range of plausible parameters and assumptions makes it difficult to pick out a specific scenario that is unambiguously recorded by the ice.

Well-defined meter-scale layering is found in only a few ice-exposing scarps, in contrast with the NPLD where meter- to decameter-scale layering is nearly ubiquitous (e.g., Herkenhoff et al., 2007). Unresolved layers (<30 cm thick) may exist at the mid-latitude scarp sites, preserving a temporal record at small scales, but the more-common crude layering may possibly be the only well-defined time signal in this ice, or the dust content of the ice may be so low or so uniform that layers are mostly not distinguishable in HiRISE images. This could indicate that the ice accumulated only under a narrow range of atmospheric conditions, while polar accumulation occurred in a wider range of

993 climates. However, surface-mantling deposits without ice exposures at latitudes <45° in
994 the mid-latitudes do show evidence of layering (Schon et al., 2009). The two scarp
995 locations with the clearest fine layering both have unconformities and crosscutting layers;
996 this may indicate that accumulation at those sites occurred at two different times possibly
997 with different climates or that some of the deposition occurred as windblown drifts rather
998 than uniform fall deposits. In both cases the uppermost material is approximately
999 horizontal and conforms to the present surface, so it was not affected significantly by
1000 aeolian transport or by ice flow, although deformation could be concentrated out of view
1001 at the base of the ice.
1002 The scarp ice likely records different climate episodes than either of the polar
1003 layered deposits. The available data are too limited to constrain any hypothesis for what
1004 orbital epochs and climate conditions might be recorded in the scarp ice other than to say
1005 that it indicates snow or frost accumulation. Part of this accumulation was likely
1006 geologically recent, since mid-latitude mantling deposits have few craters and young
1007 surface ages of a few million years (Schon et al., 2012), although the base of the deposits
1008 could be older. Harish et al. (2020) estimated the ages of two scarp-hosting craters to be
1009 25 and 95 Ma, and the surface age of one of the host mantling units to be 1 Ma. Viola et
1010 al. (2015) estimated that a mid-latitude icy deposit in the region of Milankovič crater is
1011 tens of millions of years old, and this may include the scarp-hosting ice there, although
1012 the characteristic expanded craters are less abundant in the crater interior, which could be
1013 a younger deposit (Fig. 9b). These ages are less than or comparable to the 30–100 Ma
1014 surface age of the SPLD (e.g., Koutnik et al., 2002), while the entire NPLD may date
1015 from the last several million years (e.g., Levrard et al., 2007; Byrne, 2009; Smith et al.,

2016). More important than the specific age is that deposition in the poles and mid-latitudes likely occurred under different climate regimes: the locations of net deposition or loss depend on Mars' obliquity and orbital parameters and associated climate changes (e.g., Head et al., 2003; Levrard et al., 2004; Forget et al., 2006; Byrne, 2009; Madeleine et al., 2009; 2014), so polar and mid-latitude ice accumulated at different parts of the cycle.

Overall, various observations indicate several regions of thick mid-latitude ice accumulation in the Late Amazonian. These include (1) SSE Hellas, as shown by scarps and scalloped depressions (Lefort et al., 2010; Zanetti et al., 2010); (2) western Utopia Planitia, as shown by scalloped depressions and radar reflectors (Morgenstern et al., 2007; Lefort et al., 2009; Stuurman et al., 2016); and (3) the greater Arcadia region, as shown by expanded craters and radar reflectors (Viola et al., 2015; Bramson et al., 2015) and some localized scarps. Debris-covered glaciers also indicate deposition concentrated east of Hellas, in Tempe Terra, and in the Deuteronilus and Protonilus Mensae regions (Holt et al., 2008; Plaut et al., 2009; Levy et al., 2014). Note that other major accumulations could have existed and been subsequently removed, as has occurred for some lobate debris aprons (Hauber et al., 2008). Deposition was probably not simultaneous in all of these regions, and the depositional conditions were also probably variable: ice in debris-covered glaciers and exposed in the scarps likely has a very low dust content (Campbell and Morgan, 2018; Dundas et al., 2018; Petersen et al., 2018), but the regional deposits in Utopia and Arcadia may be less ice-rich (Campbell and Morgan, 2018). No site has all of the ice indicators in abundance. Radar reflectors are sparse in SSE Hellas, although rough topography limits the detectability of possible interfaces in

that region (Cook et al., 2020). Radar loss tangents support high ice contents for debris-covered glaciers but not for the Utopia and Arcadia deposits. Scarp exposures are sparse and not found at all in some regions. Additionally, one or the other of scalloped depressions and expanded craters dominate the sublimation-thermokarst population rather than a mix occurring. These differences could reflect differences in the lithic content of the ice (including layering), overburden properties, regional topography (influencing radar clutter) or the regional climate history.

6. Conclusions

We present distributions of ice-exposing craters and large ice-exposing scarps at middle to high latitudes on Mars. Both types of feature indicate high subsurface ice contents well in excess of pore filling. Regional variations in the crater exposures suggest that high ice content is common at shallow depths at mid-latitudes (~40 °N) in the Arcadia Planitia region compared with the northern part of the Tharsis rise, where pore ice may be more common. Above ~50° latitude, clean ice exposures are very common at all longitudes. The nature of ice exposures in some of the largest craters indicates that clean ice is not a product of the impact process. Variations in crater clusters demonstrate that both ice content and the depth to ice have substantial local variability. The scarps are characteristically found between 50–61 °N/S and are concentrated at particular longitudes. They appear to form in thick surface-mantling deposits produced by past snowfall and create a distinctive category of sublimation-thermokarst landform. The latitudinal and longitudinal controls suggest that the scarps form in locations with particularly thick, clean ice deposits and are exposed by a latitude-dependent process.

Both of these types of exposures provide important constraints on the climate history of Mars as well as reference locations for other remote-sensing data sets.

Acknowledgments

Icy scarp analysis was funded by the NASA Solar System Workings Program agreement 80HQTR19T0019, and assessment of HiRISE observations of ice-exposing craters was funded by the Mars Subsurface Water Ice Mapping project (JPL subcontract JPL1639821). SJC is grateful to the French Space Agency CNES for supporting her HiRISE-related work. IJD was funded by NASA Solar System Workings grant 80NSSC20K0789. CTX, HiRISE, and CRISM targeting was funded by the Mars Reconnaissance Orbiter Project, and we thank the project operations teams for their work to acquire the data used in this study. The CTX operations team planned many images to search for new impacts and identified locations of candidates for HiRISE targeting. Jay Dickson and Mathieu Vincendon provided detailed and helpful reviews. Marc Hunter assisted with preparation of the USGS Data Release.

The Supplementary Data is also available as a USGS Data Release at https://doi.org/10.5066/P9Y8FR1R (Dundas et al., 2021). All CTX, HiRISE, and CRISM image data used are available via the Planetary Data System Imaging and Geosciences nodes (https://pds-imaging.jpl.nasa.gov/volumes/mro.html and https://pds-geosciences.wustl.edu/missions/mro/crism.htm). All map-projected HiRISE images in figures are courtesy NASA/JPL/University of Arizona, and map-projected CTX images are courtesy NASA/JPL/MSSS/University of Arizona. Controlled THEMIS mosaics are publicly available (https://astrogeology.usgs.gov/maps/mars-themis-controlled-mosaics-

and-final-smithed-kernels) via Astropedia and uncontrolled mosaics are included as layers in JMARS (http://www.mars.asu.edu/data/), which was used for analysis. The original images used in the mosaics are available via the Planetary Data System Imaging Node (https://pds-imaging.jpl.nasa.gov/volumes/ody.html). Thermal Emission Spectrometer (TES) thermal inertia data are available from the PDS Geosciences node (https://pds-geosciences.wustl.edu/missions/mgs/tes-timap.html) and albedo data at the PDS TES data node (http://tes.asu.edu/products/index.html). The use of trade, product, or firm names is for identification purposes only and does not constitute an endorsement by the U.S. Government.

References

Appéré, T., Schmitt, B., Langevin, Y., Douté, S., Pommerol, A., Forget, F., Spiga, A., Gondet, B., Bibring, J.-P. (2011). Winter and spring evolution of northern seasonal deposits on Mars from OMEGA on Mars Express. *J. Geophys. Res., 115,* E05001. https://doi.org/10.1029/2010JE003762.

Aylward, D. S., Schmidt, L. M., Levy, J. S. (2019). Formation of coarse sediment lags in ice-sediment mixtures: A geomorphic signature of sublimation on regolith surfaces. *Planet. Space Sci.*, 174, 8-13. https://doi/org/10.1016/j.pss.2019.05.006.

Bandfield, J. L. (2007). High-resolution subsurface water-ice distributions on Mars. *Nature, 447,* 64-67. https://doi.org/10.1038/nature05781.

Bandfield, J. L., & Feldman, W. C. (2008). Martian high-latitude permafrost depth and surface cover thermal inertia distributions. *J. Geophys. Res., 113,* E08001. https://doi.org/10.1029/2007JE003007.

1108 Bart, G. D. (2014). The quantitative relationship between small impact crater morphology
1109 and regolith depth. *Icarus, 235,* 130-135.
1110 https://doi.org/10.1016/j.icarus.2014.03.020.
1111 Boynton, W. V., Feldman, W. C., Squyres, S. W., Prettyman, T. H., Brückner, J., Evans,
1112 L. G., et al. (2002). Distribution of hydrogen in the near surface of Mars: Evidence
1113 for subsurface ice deposits. *Science, 297,* 81-85.
1114 https://doi.org/10.1126/science.1073722.
1115 Bramson, A. M., Byrne, S., Putzig, N. E., Sutton, S., Plaut, J. J., Brothers, T. C., & Holt,
1116 J. W. (2015). Widespread excess ice in Arcadia Planitia, Mars. *Geophys. Res. Lett.,*
1117 *42,* 6566-6574. https://doi.org/10.1002/2015GL064844.
1118 Bramson, A. M., Byrne, S., Bapst, J. (2017). Preservation of mid-latitude ice sheets on
1119 Mars. *J. Geophys. Res., 122,* 2,250-2,266. https://doi.org/10.1002/2017JE005357.
1120 Bramson, A. M., Byrne, S., Bapst, J., Smith, I. B., McClintock, T. (2019). A migration
1121 model for the polar spiral troughs of Mars. *J. Geophys. Res., 124,* 1,020-1,043.
1122 https://doi.org/10.1029/2018JE005806.
1123 Bridges, N. T., et al. (2010). Aeolian bedforms, yardangs, and indurated surfaces in the
1124 Tharsis Montes as seen by the HiRISE camera: Evidence for dust aggregates. *Icarus,*
1125 *205,* 165-182. https://doi.org/10.1016/j.icarus.2009.05.017.
1126 Buri, P., Pellicciotti, F. (2018). Aspect controls the survival of ice cliffs on debris-
1127 covered glaciers. *Proc. Nat. Acad. Sci., 115,* 4,369-4,374.
1128 https://doi.org/10.1073/pnas.1713892115.
1129 Byrne, S. (2009). The polar deposits of Mars. *Ann. Rev. Earth Planet. Sci., 37,* 535-560.
1130 https://doi.org/10.1146/annurev.earth.031208.100101.

Byrne, S., Dundas, C. M., Kennedy, M. R., Mellon, M. T., McEwen, A. S., Cull, S. C., et al. (2009). Distribution of mid-latitude ground ice on Mars from new impact craters. *Science, 325,* 1674-1676. https://doi.org/10.1126/science.1175307.

Campbell, B. A., Morgan, G. A. (2018). Fine-scale layering of Mars polar deposits and signatures of ice content in nonpolar material from multiband SHARAD data processing. *Geophys. Res. Lett., 45,* 1,759-1,766. https://doi.org/10.1002/2017GL075844.

Chamberlain, M. A., & Boynton, W. V. (2007). Response of Martian ground ice to orbit-induced climate change. *J. Geophys. Res., 112,* E06009. https://doi.org/10.1029/2006JE002801.

Christensen, P. R., Bandfield, J. L., Hamilton, V. E., Ruff, S. W., Kieffer, H. H., et al. (2001). Mars Global Surveyor Thermal Emission Spectrometer experiment: Investigation description and surface science results. *J. Geophys. Res., 106,* 23,823-23,871. https://doi.org/10.1029/2000JE001370.

Christensen, P. R., Jakosky, B. M., Kieffer, H. H., Malin, M. C., McSween, H. Y. Jr., Nealson, K., et al. (2004). The Thermal Emission Imaging System (THEMIS) for the Mars 2001 Odyssey mission. *Space Sci. Rev., 110*(1), 85-130. https://doi.org/10.1023/B:SPAC.0000021008.16305.94.

Clark, R. N., & Lucey, P. G. (1984). Spectral properties of ice-particulate mixtures and implications for remote sensing. 1. Intimate mixtures. *J. Geophys. Res., 89,* 6,341-6,348. https://doi.org/10.1029/JB089iB07p06341.

Conway, S. J., & Balme, M. R. (2014). Decameter thick remnant glacial ice deposits on Mars. *Geophys. Res. Lett., 41,* 5402-5409. https://doi.org/10.1002/2014GL060314.

1154 Cook, C. W., Bramson, A. M., Byrne, S., Holt, J. W., Christoffersen, M. S., Viola, D.,
1155 Dundas, C. M., Goudge, T. A. (2020). Sparse subsurface radar reflectors in Hellas
1156 Planitia, Mars. *Icarus*, *348*, article #113847.
1157 https://doi.org/10.1016/j.icarus.2020.113847.
1158 Cull, S., Arvidson, R. E., Mellon, M. T., Skemer, P., Shaw, A., Morris, R. V. (2010).
1159 Composition of subsurface ices at the Mars Phoenix landing site. *Geophys. Res. Lett.*,
1160 *37*, L24203. https://doi.org/10.1029/2010GL045372.
1161 Delamere, W. A., et al. (2010). Color imaging of Mars by the High Resolution Imaging
1162 Science Experiment (HiRISE). *Icarus, 205*, 38-52.
1163 https://doi.org/10.1016/j.icarus.2009.03.012.
1164 Dundas, C. M. (2017a). Effects of varying obliquity on Martian sublimation thermokarst
1165 landforms. *Icarus, 281*, 115-120. https://doi.org/10.1016/j.icarus.2016.08.031.
1166 Dundas, C. M. (2017b). Effects of lava heating on volatile-rich slopes on Io. *J. Geophys.*
1167 *Res. Planets, 122*, 546-559. https://doi.org/10.1002/2016JE005177.
1168 Dundas, C. M., Byrne, S., McEwen, A. S., Mellon, M. T., Kennedy, M. R., Daubar, I. J.,
1169 Saper, L. (2014). HiRISE observations of new impact craters exposing Martian
1170 ground ice. *J. Geophys. Res., 119*, 109-127. https://doi.org/10.1002/2013JE004482.
1171 Dundas, C. M., Byrne, S., & McEwen, A. S. (2015). Modeling the development of
1172 Martian sublimation thermokarst landforms. *Icarus*, *262*, 154-169.
1173 https://doi.org/10.1016/j.icarus.2015.07.033.
1174 Dundas, C. M., Bramson, A. M., Ojha, L., Wray, J. J., Mellon, M. T., Byrne, S., et al.
1175 (2018). Exposed subsurface ice sheets in the Martian mid-latitudes. *Science, 359*,
1176 199-201. https://doi.org/10.1126/science.aao1619.

1177 Dundas, C. M., McEwen, A. S., Diniega, S., Hansen, C. J., Byrne, S., McElwaine, J. N.
1178 (2019). The formation of gullies on Mars today. *Geol. Soc. London Spec. Pub., 467*,
1179 67-94. https://doi.org/10.1144/SP467.5.
1180 Dundas, C. M., Mellon, M. T., Conway, S. J., Daubar, I. J., Williams, K. E., Ojha, L.,
1181 Wray, J. J., Bramson, A. M., Byrne, S., McEwen, A. S., Posiolova, L. V., Speth, G.,
1182 Viola, D., Landis, M., Morgan, G. A., and Pathare, A. V. (2021). Supplementary Data
1183 for "Widespread Exposures of Extensive Clean Shallow Ice in the Mid-Latitudes of
1184 Mars": U.S. Geological Survey data release. https://doi.org/10.5066/P9Y8FR1R.
1185 Fassett, C. I., Levy, J. S., Dickson, J. L., & Head, J. W. (2014). An extended period of
1186 episodic northern mid-latitude glaciation on Mars during the Middle to Late
1187 Amazonian: Implications for long-term obliquity history. *Geology*, *42*, 763-766.
1188 https://doi.org/10.1130/G35798.1.
1189 Fergason, R. L., & Weller, L. (2019). The THEMIS controlled mosaics of Mars and final
1190 smithed kernels. 4th Planetary Data Workshop, abstract #7059.
1191 Fischer, E. M., & Pieters, C. M. (1993). The continuum slope of Mars: Bidirectional
1192 reflectance investigations and applications to Olympus Mons. *Icarus, 102*, 185-202.
1193 https://doi.org/10.1006/icar.1993.1043.
1194 Fisher, D. A. (2005). A process to make massive ice in the Martian regolith using long-
1195 term diffusion and thermal cracking. *Icarus*, *179*, 387-397.
1196 https://doi.org/10.1016/j.icarus.2005.07.024.
1197 Forget, F., Haberle, R. M., Montmessin, F., Levrard, B., Head, J. W. (2006). Formation
1198 of glaciers on Mars by atmospheric precipitation at high obliquity. *Science*, *311*, 368-
1199 371. https://doi.org/10.1126/science.1120335.

Geissler, P. E. (2014). The birth and death of transverse aeolian ridges on Mars. *J. Geophys. Res., 119,* 2583-2599. https://doi.org/10.1002.2014JE004633.

Haltigin, T., Osinski, G., Baylis, A., Barnard, I. (2018). Orbital Synthetic Aperture Radar for subsurface ice detection on Mars: Scientific rationale and Canadian technical concept. 42nd COSPAR Scientific Assembly, abstract B4.2-33-18.

Harish, Vijayan, S., Mangold, N., Bhardwaj, A. (2020). Water-ice exposing scarps within the northern mid-latitude craters on Mars. *Geophys. Res. Lett.*, 47, e2020GL089057. https://doi.org/10.1029/2020GL089057.

Hauber, E., van Gasselt, S., Chapman, M. G., Neukum, G. (2008). Geomorphic evidence for former lobate debris aprons at low latitudes on Mars: Indicators of the Martian paleoclimate. *J. Geophys. Res., 113,* E02007. https://doi.org/10.1029/2007JE002897.

Head, J. W., Mustard, J. F., Kreslavsky, M. A., Milliken, R. E., Marchant, D. R. (2003). Recent ice ages on Mars. *Nature, 426,* 797-802. https://doi.org/10.1038/nature02114.

Heldmann, J. L., Schurmeier, L., McKay, C., Davila, A., Stoker, C., Marinova, M., Wilhelm, M. B. (2014). Midlatitude ice-rich ground on Mars as a target in the search for evidence of life and for *in situ* resource utilization on human missions. *Astrobiology, 14,* 102-118. https://doi.org/10.1089/ast.2013.1103.

Herkenhoff, K. E., Byrne, S., Russell, P. S., Fishbaugh, K. E., & McEwen, A. S. (2007). Meter-scale morphology of the north polar region of Mars. *Science, 317,* 1711-1715. https://doi.org/10.1126/science.1143544.

Holt, J. W., et al. (2008). Radar sounding evidence for buried glaciers in the southern mid-latitudes of Mars. *Science, 322,* 1,235-1,238. https://doi.org/10.1126/science.1164246.

Hudson, T. L., Aharonson, O., Schorghofer, N., Farmer, C. B., Hecht, M. H., Bridges, N. T. (2007). Water vapor diffusion in Mars subsurface environments. *J. Geophys. Res.*, *112*, E05016. https://doi.org/10.1029/2006JE002815.

Hudson, T. L., Aharonson, O. (2008). Diffusion barriers at Mars surface conditions: Salt crusts, particle size mixtures, and dust. *J. Geophys. Res.*, *113*, E09008. https://doi.org/10.1029/2007JE003026.

Kerrigan, M. (2013). The periglacial landscape of Utopia Planitia: Geologic evidence for recent climate change on Mars. MS thesis, Dept. of Earth Sciences, Univ. Western Ontario, London, Ontario, Canada.

Khuller, A. R., & Christensen, P. R. (2019). Evidence of water-rich snow deposits within Martian gullies. Lunar Planet. Sci. Conf. 50, abstract #3060.

Kieffer, H. H. (2007). Cold jets in the Martian polar caps. *J. Geophys. Res.*, *112*, E08005. https://doi.org/10.1029/2006JE002816.

Kirkbride, M. P. (1993). The temporal significance of transitions from melting to calving termini at glaciers in the central Southern Alps of New Zealand. *The Holocene, 3*, 232-240. https://doi.org/10.1177/095968369300300305.

Koutnik, M., Byrne, S., Murray, B. (2002). *J. Geophys. Res. Planets*, 107, E11, 5100. https://doi.org/10.1029/2001JE001805.

Landis, M., McEwen, A. S., Daubar, I. J., Hayne, P. O., Byrne, S., Dundas, C. M., Sutton, S. S., Britton, A., Herkenhoff, K. E. (2020). South Polar Layered Deposits near-surface properties inferred from a dated impact crater. 7th Int. Conf. Mars Polar Sci. Expl., abstract #6025.

Laskar, J., Correia, A. C. M., Gastineau, M., Joutel, F., & Levrard, B. (2004). Long term evolution and chaotic diffusion of the insolation quantities of Mars. *Icarus, 170,* 343-364. https://doi.org/10.1016/j.icarus.2004.04.005.

Lefort, A., Russell, P. S., Thomas, N., McEwen, A. S., Dundas, C. M., & Kirk, R. L. (2009). Observations of periglacial landforms in Utopia Planitia with the High Resolution Imaging Science Experiment (HiRISE). *J. Geophys. Res., 114,* E04005. https://doi.org/10.1029/2008JE003264.

Lefort, A., Russell, P. S., & Thomas, N. (2010). Scalloped terrains in the Peneus and Amphitrites Paterae region of Mars as observed by HiRISE. *Icarus, 205,* 259-268. https://doi.org/10.1016/j.icarus.2009.06.005.

Leighton, R. B., & Murray, B. C. (1966). Behavior of carbon dioxide and other volatiles on Mars. *Science, 153,* 136-144. https://doi.org/10.1126/science.153.3732.136.

Levrard, B., Forget, F., Montmessin, F., Laskar, J. (2004). Recent ice-rich deposits formed at high latitudes on Mars by sublimation of unstable equatorial ice during low obliquity. *Nature, 431,* 1,072-1,075. https://doi.org/10.1038/nature03055.

Levrard, B., Forget, F., Montmessin, F., Laskar, J. (2007). Recent formation and evolution of northern Martian polar layered deposits as inferred from a global climate model. *J. Geophys. Res., 112,* E06012. https://doi.org/10.1029/2006JE002772.

Levy, J. S., Head, J., Marchant, D. (2009a). Thermal contraction crack polygons on Mars: Classification, distribution, and climate implications from HiRISE observations. *J. Geophys. Res., 114,* E01007. https://doi.org/10.1029/2008JE003273.

Levy, J. S., Head, J., Marchant, D. (2009b). Concentric crater fill in Utopia Planitia: History and interaction between glacial “brain terrain” and periglacial mantle processes. *Icarus, 202,* 462-476. https://doi.org/10.1016/j.icarus.2009.02.018.

Levy, J. S., Fountain, A. G., Dickson, J. L., Head, J. W., Okal, M., Marchant, D. R., Watters, J. (2013). Accelerated thermokarst formation in the McMurdo Dry Valleys, Antarctica. *Sci. Rep., 3,* 2269. https://doi.org/10.1038/srep02269.

Levy, J. S., Fassett, C. I., Head, J. W., Schwartz, C., Watters, J. L. (2014). Sequestered ice contribution to the global Martian water budget: Geometric constraints on the volume of remnant, midlatitude debris-covered glaciers. *J. Geophys. Res., 119,* 2,188-2,196. https://doi.org/10.1002/2014JE004685.

Madeleine, J.-B., Forget, F., Head, J. W., Levrard, B., Montmessin, F., Millour, E. (2009). Amazonian northern mid-latitude glaciation on Mars: A proposed climate scenario. *Icarus, 203,* 390-405. https://doi.org/10.1016/j.icarus.2009.04.037.

Madeleine, J.-B., Head, J. W., Forget, F., Navarro, T., Millour, E., Spiga, A., Colaïtis, A., Määttänen, A., Montmessin, F., & Dickson, J. L. (2014). Recent Ice Ages on Mars: The role of radiatively active clouds and cloud microphysics. *Geophys. Res. Lett., 41,* 4873-4879. https://doi.org/10.1002/2014GL059861.

Malin, M. C., Bell, J. F., Cantor, B. A., Caplinger, M. A., Calvin, W. M., et al. (2007). Context Camera investigation on board the Mars Reconnaissance Orbiter. *J. Geophys. Res., 112,* E05S04. https://doi.org/10.1029/2006JE002808.

Mangold, N. (2005). High latitude patterned grounds on Mars: Classification, distribution and climatic control. *Icarus, 174,* 336-359. https://doi.org/10.1016/j.icarus.2004.07.030.

McEwen, A. S., Eliason, E. M., Bergstrom, J. W., Bridges, N. T., Hansen, C. J., et al. (2007). Mars Reconnaissance Orbiter's High Resolution Imaging Science Experiment. *J. Geophys. Res., 112,* E05S02. https://doi.org/10.1029/2005JE002605.

Mellon, M. T. (1997). Small-scale polygonal features on Mars: Seasonal thermal contraction cracks in permafrost. *J. Geophys. Res., 102,* 25,617-25,628. https://doi.org/10.1029/97JE02582.

Mellon, M. T., & Jakosky, B. M. (1993). Geographic variations in the thermal and diffusive stability of ground ice on Mars. *J. Geophys. Res., 98,* 3345-3364. https://doi.org/10.1029/92JE02355.

Mellon, M. T., & Jakosky, B. M. (1995). The distribution and behavior of Martian ground ice during past and present epochs. *J. Geophys. Res., 100,* 11,781-11,799. https://doi.org/10.1029/95JE01027.

Mellon, M. T., Feldman, W. C., & Prettyman, T. H. (2004). The presence and stability of ground ice in the southern hemisphere of Mars. *Icarus, 169,* 324-340. https://doi.org/10.1016/j.icarus.2003.10.022.

Mellon, M. T., Arvidson, R. E., Sizemore, H. G., Searls, M. L., Blaney, D. L., Cull, S., et al. (2009). Ground ice at the Phoenix landing site: Stability state and origin. *J. Geophys. Res., 114,* E00E07. https://doi.org/10.1029/2009JE003417.

Melosh, H. J. (1989). Impact Cratering: A Geologic Process. New York: Oxford University Press.

MEPAG ICE-SAG Report (2019). Report from the Ice and Climate Evolution Science Analysis Group (ICE-SAG). S. Diniega and N. E. Putzig (chairs), 157 pages posted 8

July 2019 by the Mars Exploration Program Analysis Group (MEPAG) at http://mepag.nasa.gov/reports.cfm.

Milliken, R. A., Mustard, J. F., & Goldsby, D. L. (2003). Viscous flow features on the surface of Mars: Observations from high-resolution Mars Orbiter Camera (MOC) images. *J. Geophys. Res.*, *108*, 5057. https://doi.org/10.1029/2002JE002005.

Mitrofanov, I. G., Malakhov, A. V., Golovin, D. V., Litvak, M. L., Sanin, A. B., Mokrousov, M. I. (2018). Neutron mapping of Mars with high spatial resolution: First results of the FREND experiment of the ExoMars project. Proceedings of the Russian Academy of Science, the Branch of Physical Science.

Morgan, G. A., et al. (2020). Subsurface water ice mapping (SWIM) on Mars: Radar surface reflectivity. Lunar Planet. Sci. Conf. 51, abstract #2790.

Morgenstern, A., Hauber, E., Reiss, D., van Gasselt, S., Grosse, G., Schirrmeister, L. (2007). Deposition and degradation of a volatile-rich later in Utopia Planitia and implications for climate history on Mars. *J. Geophys. Res.*, *112*, E06010. https://doi.org/10.1029/2006JE002869.

Mouginot, J., Pommerol, A., Kofman, W., Beck, P., Schmitt, B., Herique, A., Grima, C., Safaeinili, A., & Plaut, J. J. (2010). The 3-5 MHz global reflectivity map of Mars by MARSIS/Mars Express: Implications for the current inventory of subsurface H_2O. *Icarus*, *210*, 612-625. https://doi.org/10.1016/j.icarus.2010.07.003.

Murray, B. C., Ward, W. R., & Yeung, S. C. (1973). Periodic insolation variations on Mars. *Science*, *180*, 638-640. https://doi.org/10.1126/science.180.4086.638.

Mustard, J. F., Cooper, C. D., Rifkin, M. K. (2001). Evidence for recent climate change on Mars from the identification of youthful near-surface ground ice. *Nature, 412,* 411-414. https://doi.org/10.1038/35086515.

Noe Dobrea, E. Z., Asphaug, E., Grant, J. A., Kessler, M. A., Mellon, M. T. (2007). Patterned ground as an alternative explanation for the formation of brain coral textures in the mid latitudes of Mars: HiRISE observations of lineated valley fill textures. 7th Int. Conf. Mars, abstract #3358.

Orloff, T. C., Kreslavsky, M. A., Asphaug, E. I. (2013). Possible mechanism of boulder clustering on Mars. *Icarus, 225,* 992-999. https://doi.org/10.1016/j.icarus.2013.01.002.

Pathare, A. V., Feldman, W. C., Prettyman, T. H., & Maurice, S. (2018). Driven by excess? Climatic implications of new global mapping of near-surface water-equivalent hydrogen on Mars. *Icarus, 301,* 97-116. https://doi.org/10.1016/j.icarus.2017.09.031.

Petersen, E. I., Holt, J. W., & Levy, J. S. (2018). High ice purity of Martian lobate debris aprons at the regional scale: Evidence from an orbital radar sounding survey in Deuteronilus and Protonilus Mensae. *Geophys. Res. Lett., 45,* 11,595-11,604. https://doi.org/10.1029/2018GL079759.

Picardi, G., et al. (2005). Radar soundings of the subsurface of Mars. *Science, 310,* 1,925-1,928. https://doi.org/10.1126/science.1122165.

Pilorget, C., & Forget, F. (2016). Formation of gullies on Mars by debris flows triggered by CO_2 sublimation. *Nature Geosci., 9,* 65-69. https://doi.org/10.1038/NGEO2619.

1354 Piqueux, S., Buz, J., Edwards, C. S., Bandfield, J. L., Kleinböhl, A., Kass, D. M., Hayne,
1355 P. O., & the MCS and THEMIS teams (2019). Widespread shallow water ice on Mars
1356 at high latitudes and mid latitudes. *Geophys. Res. Lett., 46,* 14,290-14,298.
1357 https://doi.org/10.1029/2019GL083947.
1358 Plaut, J. J., et al. (2007). Subsurface radar sounding of the south polar layered deposits of
1359 Mars. *Science, 316,* 92-95. https://doi.org/10.1126/science.1139672.
1360 Plaut, J. J., Safaeinili, A., Holt, J. W., Phillips, R. J., Head, J. W., Seu, R., Putzig, N. E.,
1361 & Frigeri, A. (2009). Radar evidence for ice in lobate debris aprons in the mid-
1362 northern latitudes of Mars. *Geophys. Res. Lett., 36,* L02203.
1363 https://doi.org/10.1029/2008GL036379.
1364 Putzig, N. E., & Mellon, M. T. (2007). Apparent thermal inertia and the surface
1365 heterogeneity of Mars. *Icarus, 191,* 68-94.
1366 https://doi.org/10.1016/j.icarus.2007.05.013.
1367 Putzig, N. E., et al. (2019). Results of the Mars Subsurface Water Ice Mapping (SWIM)
1368 project. 9th Int. Mars Conference, abstract #6427.
1369 Putzig, N. E., et al. (2020). Subsurface Water Ice Mapping (SWIM) on Mars to support in
1370 situ resource utilization. Lunar and Planetary Science Conference 51, abstract #2648.
1371 Quaide, W. L., Oberbeck, V. R. (1968). Thickness determination of the lunar surface
1372 layer from lunar impact craters. *J. Geophys. Res., 73,* 5,247-5,270.
1373 https://doi.org/10.1029/JB073i016p05247.
1374 Reufer, A., Thomas, N., Benz, W., Byrne, S., Bray, V., Dundas, C., & Searls, M. (2010).
1375 Models of high velocity impacts into dust-covered ice: Application to Martian

northern lowlands. *Planet. Space Sci.*, *58*, 1160-1168. https://doi.org/10.1016/j.pss.2010.04.008.

Rice, M. S., Bell, J. F., Cloutis, E. A., Wray, J. J., Herkenhoff, K. E., Sullivan, R., Johnson, J. R., & Anderson, R. B. (2011). Temporal observations of bright soil exposures at Gusev crater, Mars. *J. Geophys. Res.*, *116*, E00F14. https://doi.org/10.1029/2010JE003683.

Ruff, S. W., & Christensen, P. R. (2002). Bright and dark regions on Mars: Particle size and mineralogical characteristics based on Thermal Emission Spectrometer data. *J. Geophys. Res.*, *107*, E12, 5127. https://doi.org/10.1029/2001JE001580.

Russell, P., et al. (2008). Seasonally active frost-dust avalanches on a north polar scarp of Mars captured by HiRISE. *Geophys. Res. Lett.*, *35*, L23204. https://doi.org/10.1029/2008GL035790.

Sakai, A., Nakawo, M., Fujita, K. (2002). Distribution characteristics and energy balance of ice cliffs on debris-covered glaciers, Nepal Himalaya. *Arctic, Antarctic and Alpine Research*, *34*, 12-19. https://doi.org/10.1080/15230430.2002.12003463.

Schon, S. C., Head, J. W., Milliken, R. E. (2009). A recent ice age on Mars: Evidence for climate oscillations from regional layering in mid-latitude mantling deposits. *Geophys. Res. Lett.*, *36*, L15202. https://doi.org/10.1029/2009GL038554.

Schon, S. C., Head, J. W., Fassett, C. I. (2012). Recent high-latitude resurfacing by a climate-related latitude-dependent mantle: Constraining age of emplacement from counts of small craters. *Planet. Space Sci.*, *69*, 49-61. https://doi.org/10.1016/j.pss.2012.03.015.

1398 Schorghofer, N., & Aharonson, O. (2005). Stability and exchange of subsurface ice on
1399 Mars. *J. Geophys. Res., 110,* E05003. https://doi.org/10.1029/2004JE002350.
1400 Schorghofer, N., & Forget, F. (2012). History and anatomy of subsurface ice on Mars.
1401 *Icarus, 220,* 1112-1120. https://doi.org/10.1016/j.icarus.2012.07.003.
1402 Sizemore, H. G., & Mellon, M. T. (2006). Effects of soil heterogeneity on Martian
1403 ground-ice stability and orbital estimates of ice table depth. *Icarus, 185,* 358-369.
1404 https://doi.org/10.1016/j.icarus.2006.07.018.
1405 Sizemore, H. G., Zent, A. P., & Rempel, A. W. (2015). Initiation and growth of Martian
1406 ice lenses. *Icarus, 251,* 191-210. https://doi.org/10.1016/j.icarus.2014.04.013.
1407 Smith, I. B., Putzig, N. E., Holt, J. W., Phillips, R. J. (2016). An ice age recorded in the
1408 polar deposits of Mars. *Science, 352,* 1075-1079.
1409 https://doi.org/10.1126/science.aad6968.
1410 Smith, I. B., Diniega, S., Beaty, D. W., Thorsteinsson, T., Becerra, P., Bramson, A. M., et
1411 al. (2018). 6th International Conference on Mars Polar Science and Exploration:
1412 Conference summary and five top questions. *Icarus, 308,* 2-14.
1413 https://doi.org/10.1016/j.icarus.2017.06.027.
1414 Smith, P. H., Tamppari, L. K., Arvidson, R. E., Bass, D., Blaney, D., Boynton, W. V., et
1415 al. (2009). H_2O at the Phoenix landing site. *Science, 325,* 58-61.
1416 https://doi.org/10.1126/science.1172339.
1417 Soare, R. J., Osinski, G. R., Roehm, C. L. (2008). Thermokarst lakes and ponds on Mars
1418 in the very recent (Late Amazonian) past. *Earth Planet. Sci. Lett., 272,* 382-393.
1419 https://doi.org/10.1016/j.epsl.2008.05.010.

Soderblom, L. A., Kreidler, T. J., Masursky, H. (1973). Latitudinal distribution of a debris mantle on the Martian surface. *J. Geophys. Res., 78*, 4,117-4,122. https://doi.org/10.1029/JB078i020p04117.

Squyres, S. W. (1978). Martian fretted terrain: Flow of erosional debris. *Icarus, 34*, 600-613. https://doi.org/10.1016/0019-5(78)90048-9.

Squyres, S. W., Carr, M. H. (1986). Geomorphic evidence for the distribution of ground ice on Mars. *Science, 231*, 249-252. https://doi.org/10.1126/science.231.4735.249.

Steele, L. J., Balme, M. R., & Lewis, S. R. (2017). Regolith-atmosphere exchange of water in Mars' recent past. *Icarus, 284*, 233-248. https://doi.org/10.1016/j.icarus.2016.11.023.

Stuurman, C. M., Osinski, G. R., Holt, J. W., Levy, J. S., Brothers, T. C., Kerrigan, M., & Campbell, B. A. (2016). SHARAD detection and characterization of subsurface water ice deposits in Utopia Planitia, Mars. *Geophys. Res. Lett., 43*, 9484-9491, https://doi.org/10.1002/2016GL070138.

van Everdingen, R. O., ed. (1998, revised 2005). Multi-language glossary of permafrost and related ground-ice terms. International Permafrost Association, 159 pages.

Vincendon, M., Forget, F., Mustard, J. (2010). Water ice at low to midlatitudes on Mars. *J. Geophys. Res.*, *115*, E10001. https://doi.org/10.1029/2010JE003584.

Viola, D., McEwen, A. S. (2018). Geomorphological evidence for shallow ice in the southern hemisphere of Mars. *Geophys. Res. Lett, 123*, 262-277. https://doi.org/10.1002/2017JE005366.

Viola, D., McEwen, A. S., Dundas, C. M., & Byrne, S. (2015). Expanded secondary craters in the Arcadia Planitia region, Mars: Evidence for tens of Myr-old shallow subsurface ice. *Icarus, 248,* 190-204. https://doi.org/10.1016/j.icarus.2014.10.032.

Ward, W. R. (1973). Large-scale variations in the obliquity of Mars. *Science, 181,* 260-262. https://doi.org/10.1126/science.181.4096.260.

Wells, E. N., Veverka, J., & Thomas, P. (1984). Mars: Experimental study of albedo changes caused by dust fallout. *Icarus, 58,* 331-338. https://doi.org/10.1016/0019-1035(84)90079-4.

Zanetti, M., Hiesinger, H., Reiss, D., Hauber, E., & Neukum, G. (2010). Distribution and evolution of scalloped terrain in the southern hemisphere, Mars. *Icarus, 206,* 691-706. https://doi.org/10.1016/j.icarus.2009.09.010.

Zuber, M. T., Phillips, R. J., Andrews-Hanna, J. C., Asmar, S. W., Konopliv, A. S., Lemoine, F. G., Plaut, J. J., Smith, D. E., & Smrekar, S. E. (2007). Density of Mars' south polar layered deposits. *Science, 317,* 1718-1719. https://doi.org/10.1126/science.1146995.

Table 1. Depths to Strong Layer at Impact Sites with Icy Color

Latitude	Longitude	N	Mean depth to ice (m)	Range
46.35°	176.89°	6	0.42	0.28 – 0.58
44.22°	164.20°	5	0.47	0.26 – 0.55
50.51°	265.2°	3	0.42	0.32 – 0.62
39.11°	190.25°	2	0.90	0.69 – 1.1
47.43°	112.01°	2	0.50	0.40 – 0.60

Planetocentric latitude, east longitude. N is the number of craters with morphologies indicating weak-over-strong layering, which are not necessarily those with visible ice. Values are given to two significant figures for relative comparison but for typical crater sizes, the potential measurement error on an individual crater is ±~30% assuming half-pixel errors in opposite directions for the rim and floor diameter. The range is the spread between the largest and smallest measurements and does not include measurement uncertainty.

Figures and Captions

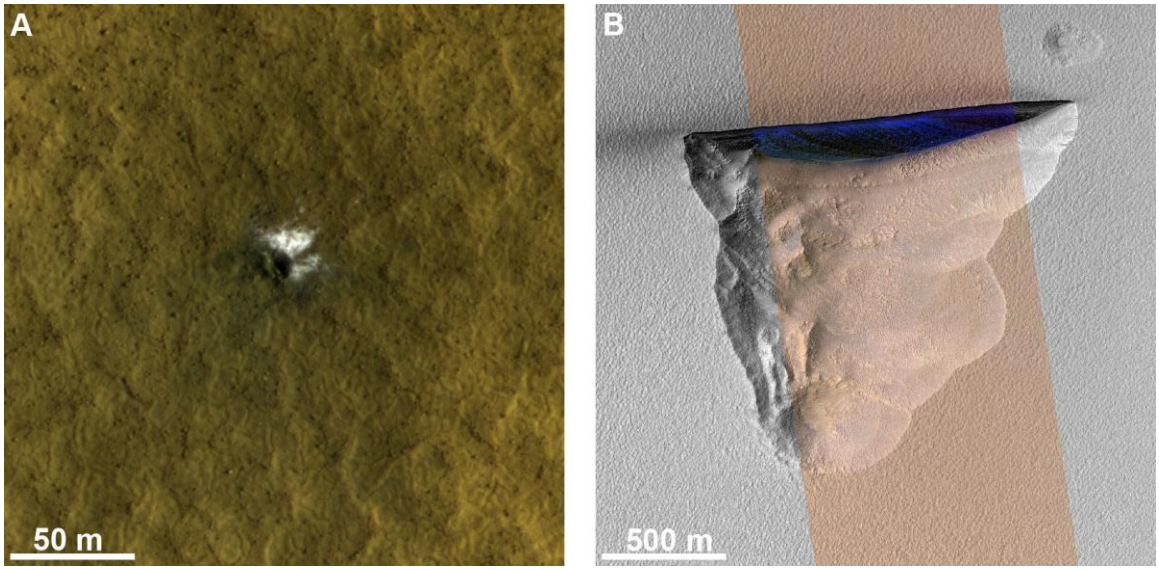

Figure 1. A) Example of an ice-exposing crater (69.3 °N, 142.2 °E). Note patchy, bright, relatively white ejecta, suggesting that this crater excavated both regolith and clean ice, as well as polygonal patterns consistent with thermal contraction cracks. B) Southern hemisphere ice-exposing scarp #6 (56.9 °S, 96.3 °E). Note distinct relatively blue coloration confined to the scarp face, which is approximately straight, sharp-edged, and faces the pole. (A: HiRISE image ESP_046189_2495, acquired at L_S=163°. Illumination is from the right and north is to the lower left (polar stereographic projection). B: HiRISE image ESP_057466_1230, acquired at L_S=279°. Illumination is from the upper left and north is up. All image figures herein are map projected in equirectangular projection with north up unless otherwise noted, and colors are enhanced as described in the text.)

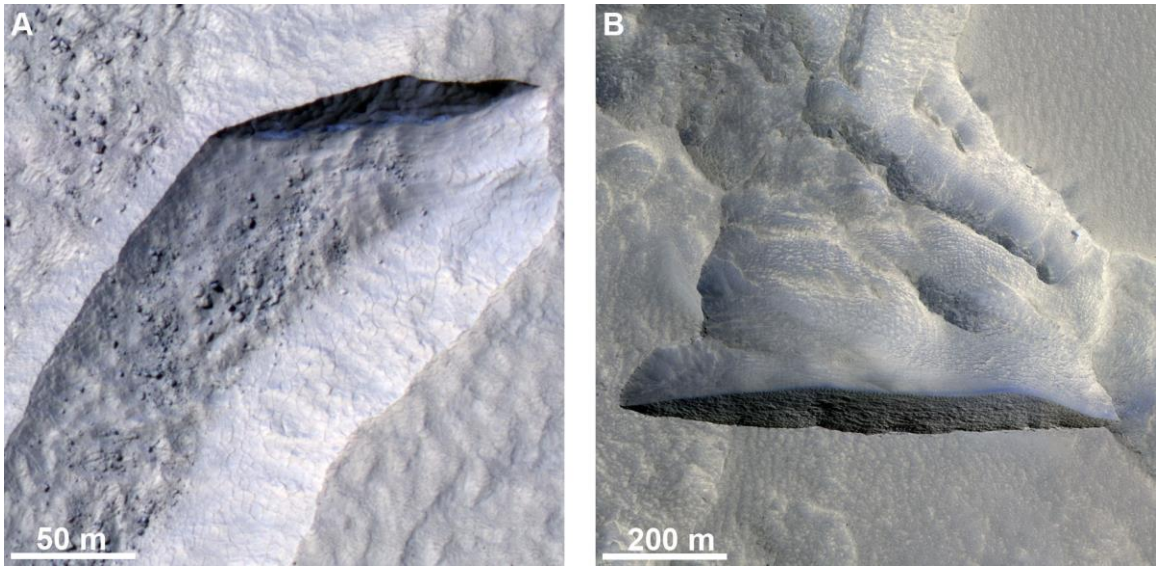

Figure 2. A) Example of a confirmed but marginal icy scarp (southern hemisphere scarp #13), where there is weak coloration of relatively blue material confined to only portions of the scarp face. B) Example of a scarp that has the morphology of an ice exposure but lacks the coloration. These are interpreted to represent the results of the same geomorphic processes that create distinctively colored scarps, but with coloration suppressed by a thin lag or somewhat higher lithic content. (A: HiRISE image ESP_057901_1235 (56.2 °S, 103.1 °E), acquired at L_S=299°. B: HiRISE image ESP_052529_2345 (54.1 °N, 212.1 °E), acquired at L_S=72°. Illumination is from the upper (A) and lower (B) left.)

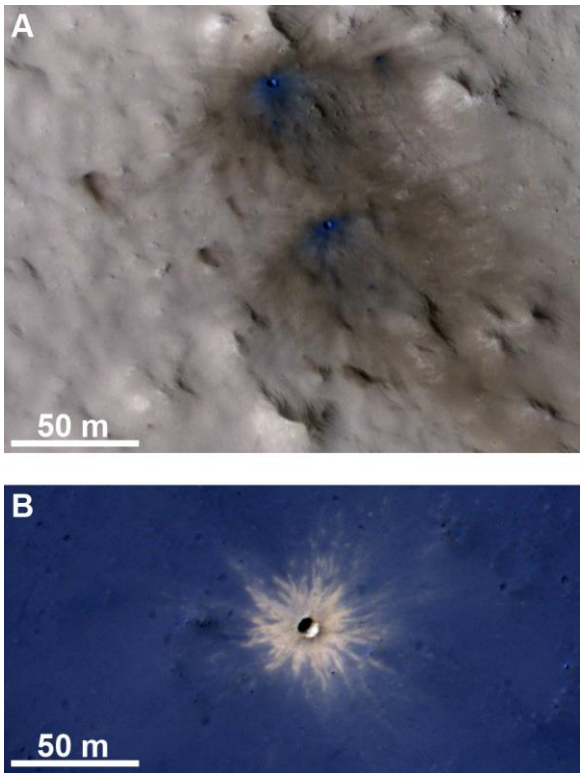

Figure 3. Examples of new craters with distinctive ejecta that are *not* interpreted as ice indicators. A) Cluster of craters with relatively blue ejecta that is not notably bright or distinctive; this coloration is consistent with mafic material exposed by the impact. B) Crater with relatively bright ejecta. This material appears relatively yellow (bright in the HiRISE red filter) rather than blue or white, and all excavated material appears bright even though any ice present at this latitude should lie beneath a debris cover. In neither case is nearby geomorphology suggestive of ice-rich material, and these latitudes do not theoretically favor shallow stable ice. (A: HiRISE image ESP_055383_2135 (33.2 °N, 58.1 °E), acquired at L_S=179°. B: HiRISE image ESP_044875_1650 (14.7 °S, 30.9 °E), acquired at L_S=112°. Illumination is from the lower (A) and upper (B) left.)

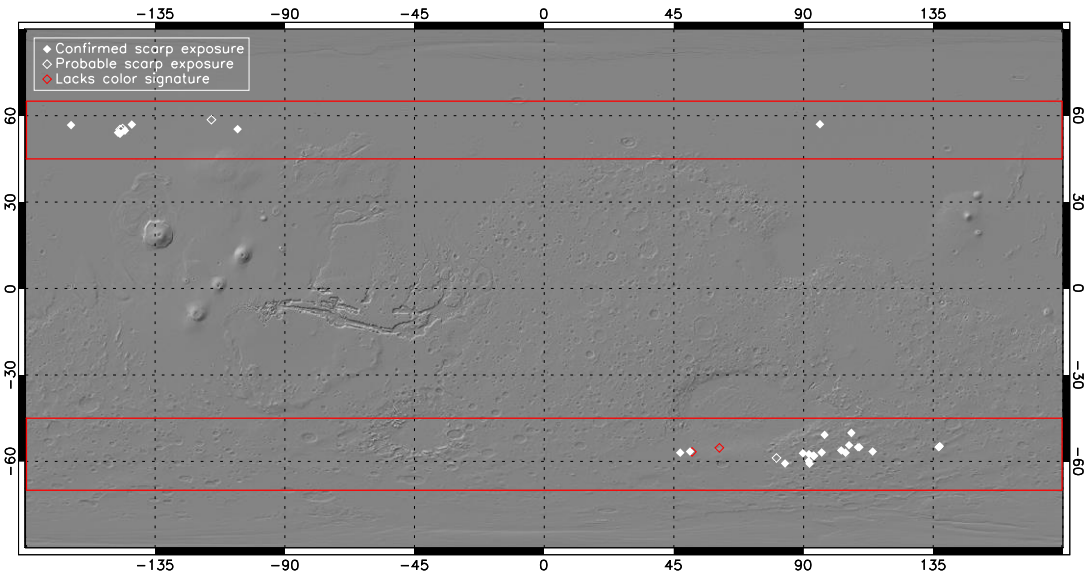

Figure 4. Map of ice-exposing scarp locations identified between 45–70 °S and 45–65 °N. Confirmed scarps (relatively blue in HiRISE) are shown as solid symbols and probable scarps are open. Some symbols overlap. Red boxes outline the survey areas. Base map is shaded relief derived from the Mars Orbiter Laser Altimeter (MOLA) digital elevation model in simple cylindrical projection.

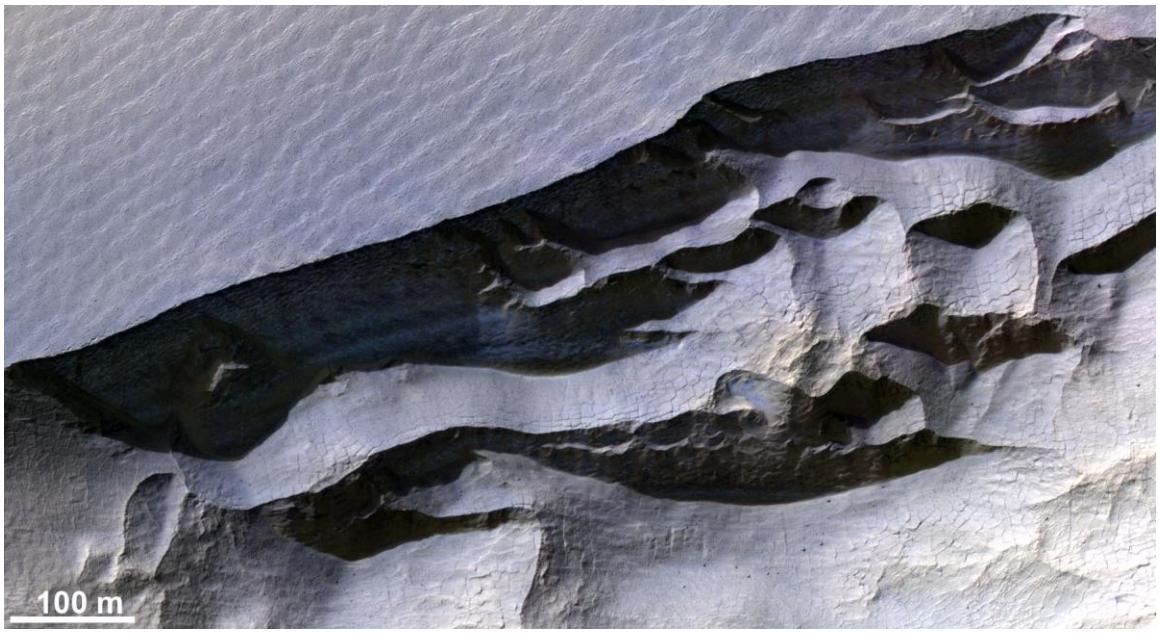

Figure 5. Southern-hemisphere scarp #15 (56.6 °S, 50.6 °E) has a complex structure. The primary scarp face and best ice exposure is largely in shadow. However, small parallel facets exist within the material at the base of the scarp. This demonstrates a high ice content within the residual material (the scarp did not erode to the base of the ice) and complex dynamics of reactivation. (HiRISE image ESP_058971_1230, acquired at L_S=346°. Illumination is from the upper left.)

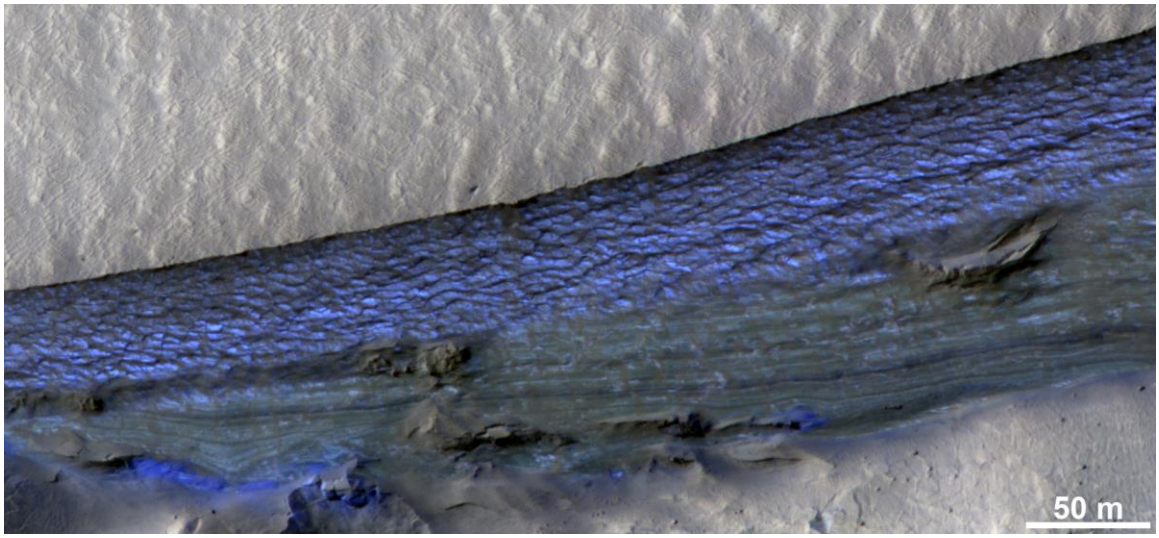

Figure 6. Contrasting layering styles in southern-hemisphere scarp #7 (57.5 °S, 91.9 °E). The lower slope (bottom of the image) shows a rare example of fine layering. The upper slope has a blocky and fractured appearance with some hints of horizontal banding, which is the typical appearance of most scarps. (HiRISE image ESP_057321_1220, acquired at L_S=272°. Illumination is from the upper left.)

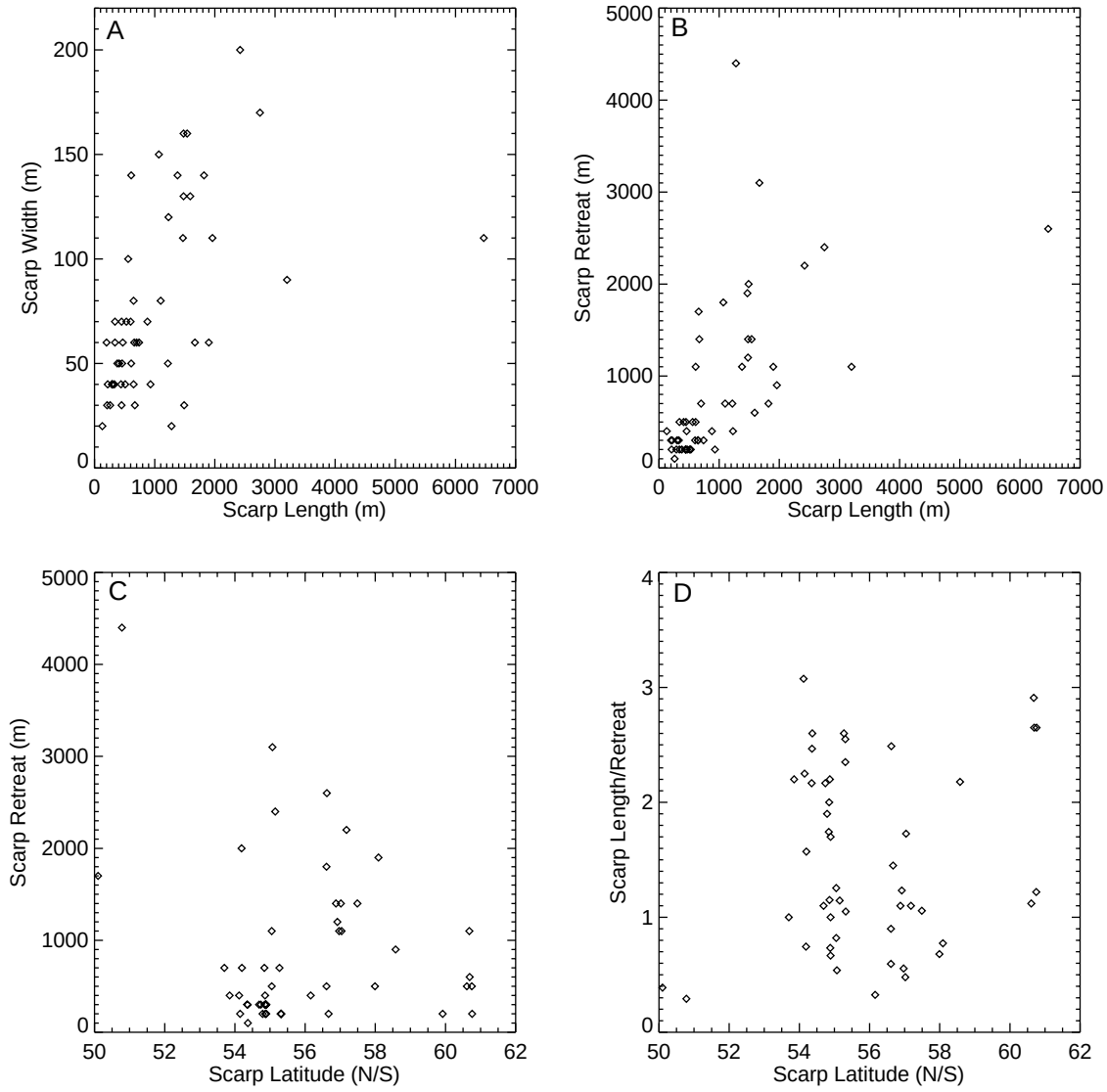

1517

1518 **Figure 7.** Quantitative morphometry of ice-exposing scarps. A) Scarp plan-view width

1519 (crest to base) versus end-to-end length. B) Scarp retreat distance versus end-to-end

1520 length. Both A and B show that wider scarps are generally taller and have retreated

1521 further. C) Scarp retreat distance versus latitude. The upper envelope of retreat distance

1522 decreases with increasing latitude. D) Pit aspect ratio (scarp length divided by retreat

1523 distance) versus latitude. All plots include data for confirmed scarps in both hemispheres.

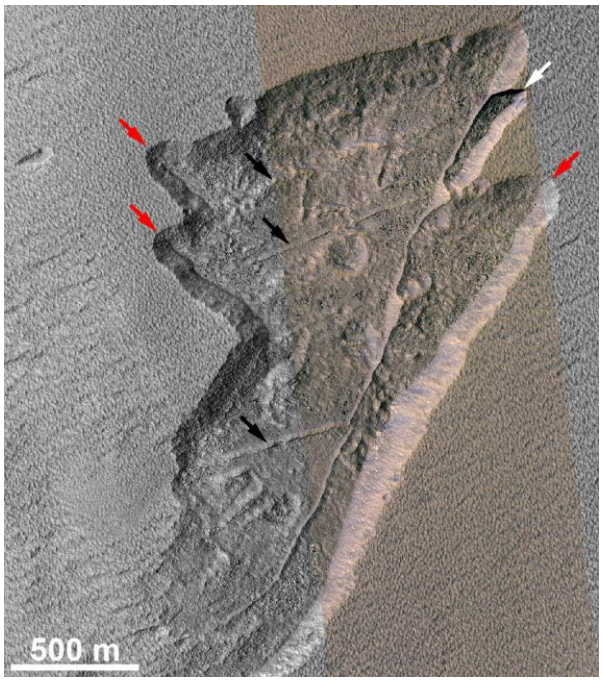

Figure 8. The pit containing southern-hemisphere scarp #13 (white arrow; see Fig. 2a for detail) reveals details of the scarp retreat process. Based on crosscutting relationships and the typical scarp geometry, the scarp initiated in the lower left part of the image and retreated approximately equatorward. It maintained the same approximate orientation throughout, as shown by several scarp-parallel ridges (black arrows). However, retreat may have been oblique rather than scarp-normal at times, since the scarp walls in the southern part of the pit are parallel but are not normal to the scarp. Multiple notches in the pit walls (red arrows) demonstrate that the scarp width varied over time and that the outer parts sometimes became inactive. It is possible that the entire scarp deactivated and only the central sections subsequently resumed retreating. Finally, secondary scarps such as the current scarp reactivated on the east side of the pit, producing a younger ridge that defines the old edge of the pit. (HiRISE image ESP_057901_1235 (56.2 °S, 103.1 °E), acquired at L_S=299°. Illumination is from the upper left.)

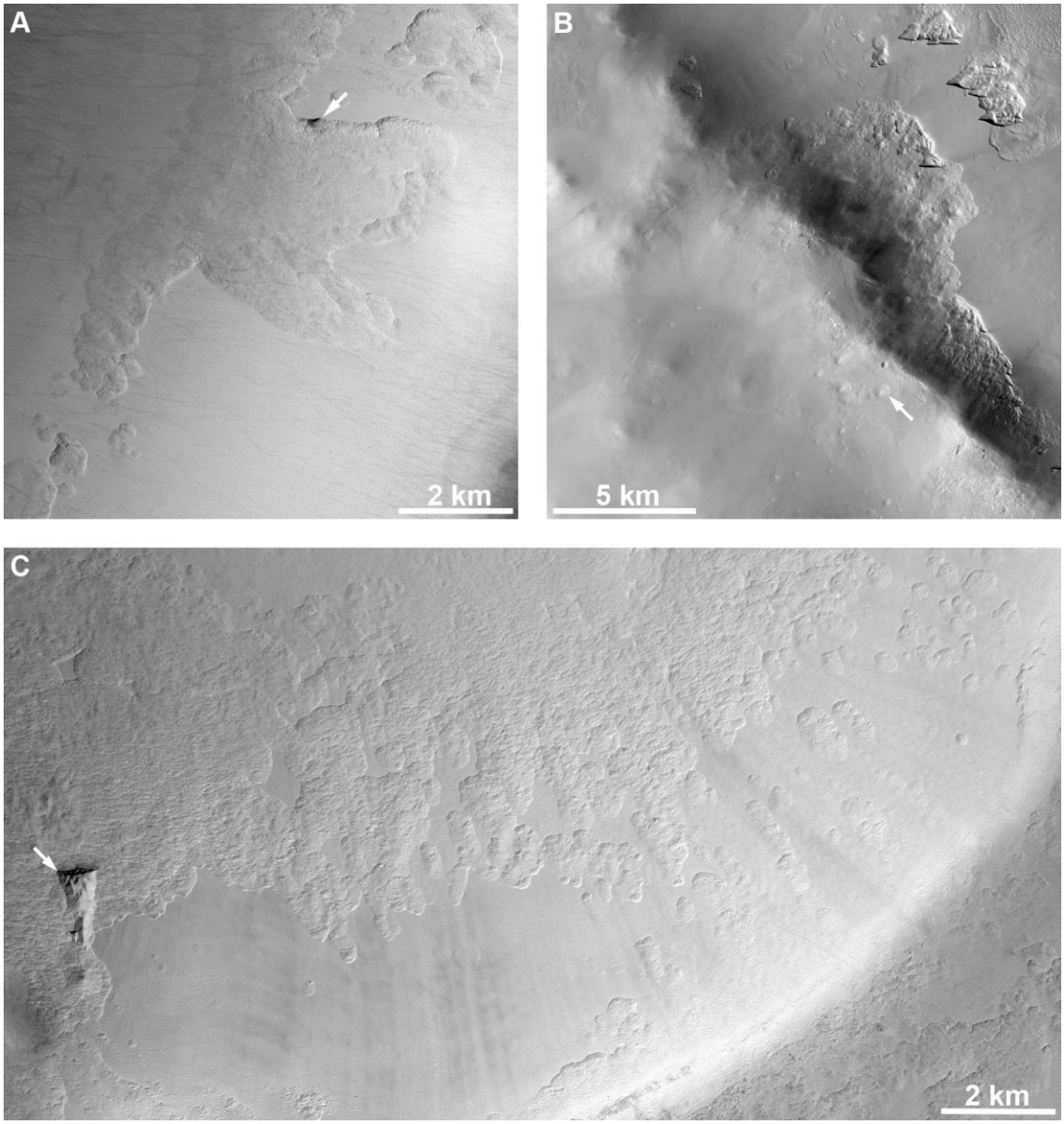

Figure 9. Scalloped depressions and ice-loss landforms. A) Probable ice-exposing southern-hemisphere scarp #18 (arrow; 58.8 °S, 80.6 °E) eroding into a mantling unit that is also being removed to form scalloped depressions. The scarp resembles parts of the scalloped depressions but is the most-shadowed (steepest) slope in the area. B) A group of scarps in southwestern Milankovič crater (54 °N, 212 °E) with expanded craters nearby (arrow indicates a prominent example). Although both occur in mantling

materials, the scarps are concentrated inside the crater rim and the craters beyond it. C) Southern-hemisphere ice-exposing scarp #14 (arrow) occurs in the vicinity of classic scalloped depressions prominent in the eastern part of the image (57 °S, 47.2 °E). The well-defined scallops are within a pristine mantling unit while the scarp is cut into partially degraded material that may have been previously dissected by scallop formation. Note that the triangular scarp-pit morphology is distinct from the scalloped depressions in shape and scale. (A: CTX image B10_013661_1211_XN_58S279W. Illumination is from the upper left. B: CTX image J22_053320_2345_XN_54N148W. Illumination from the lower left. C: CTX image K11_057692_1221_XN_57S312W. Illumination is from the upper left.)

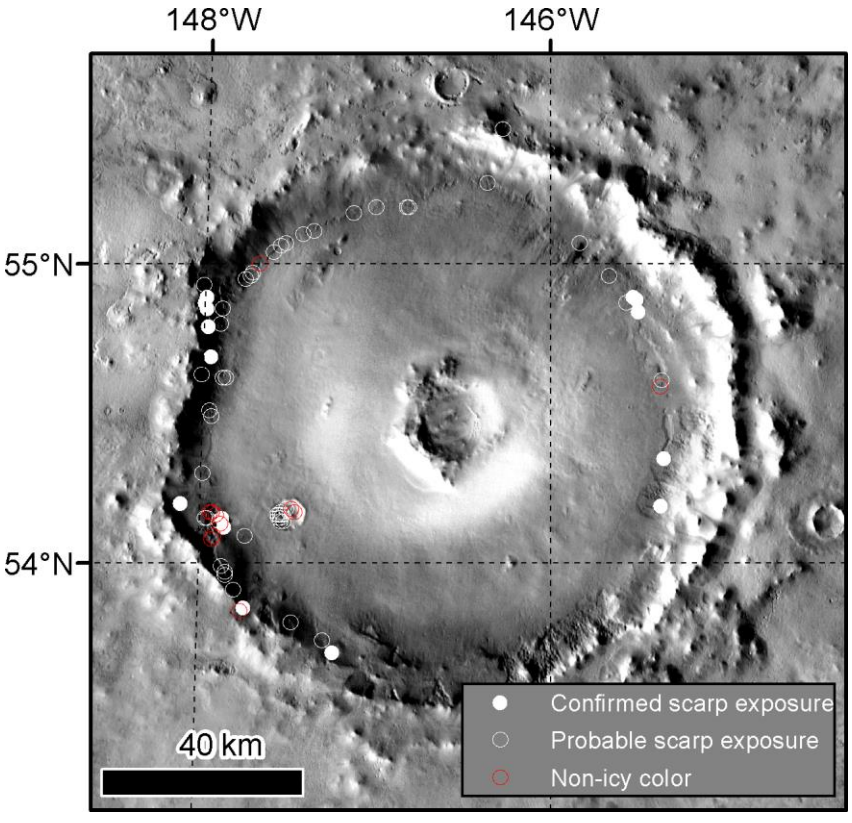

Figure 10. Map of scarps in Milankovič crater. Solid white circles show confirmed icy scarps, open white circles are classified as probable, and red symbols have the morphology of icy scarps but lack the coloration in HiRISE images. Scarps generally line the base of the crater rim, apart from a cluster in a smaller crater within Milankovič. Base map is the THEMIS controlled mosaic in sinusoidal projection centered on 146 °W.

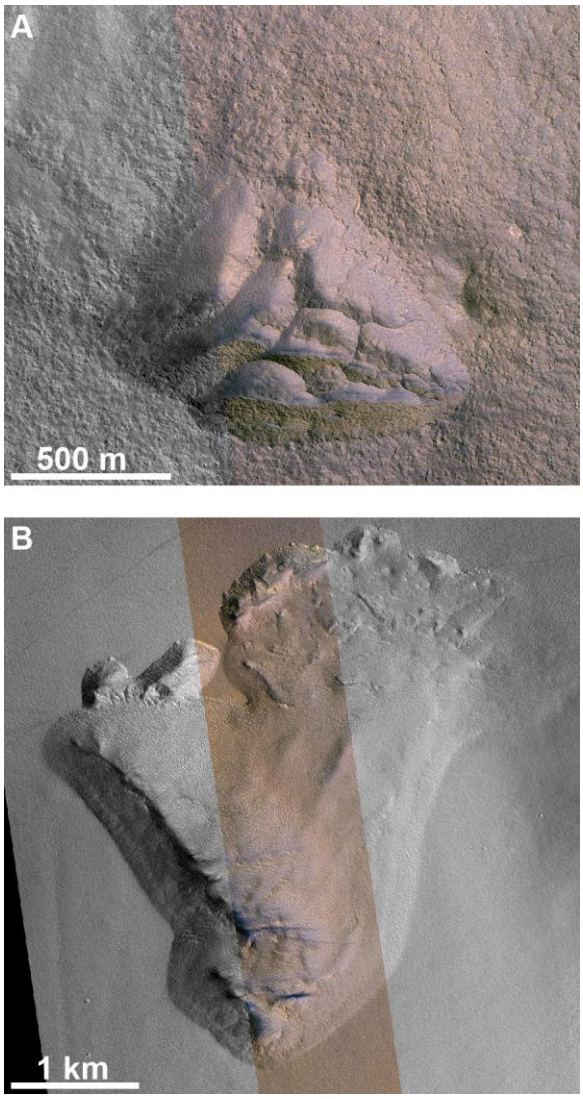

Figure 11. Pits with morphologies similar to ice-exposing scarp locations, but without well-defined scarps or distinct relatively blue exposures. (A: HiRISE image ESP_061998_2405 (60.4 °N, 197.8 °E), acquired at L_S=95°. B: HiRISE image

ESP_057176_1255 (54 °S, 90.2 °E), acquired at L_S=265°. Illumination is from the left in both panels.)

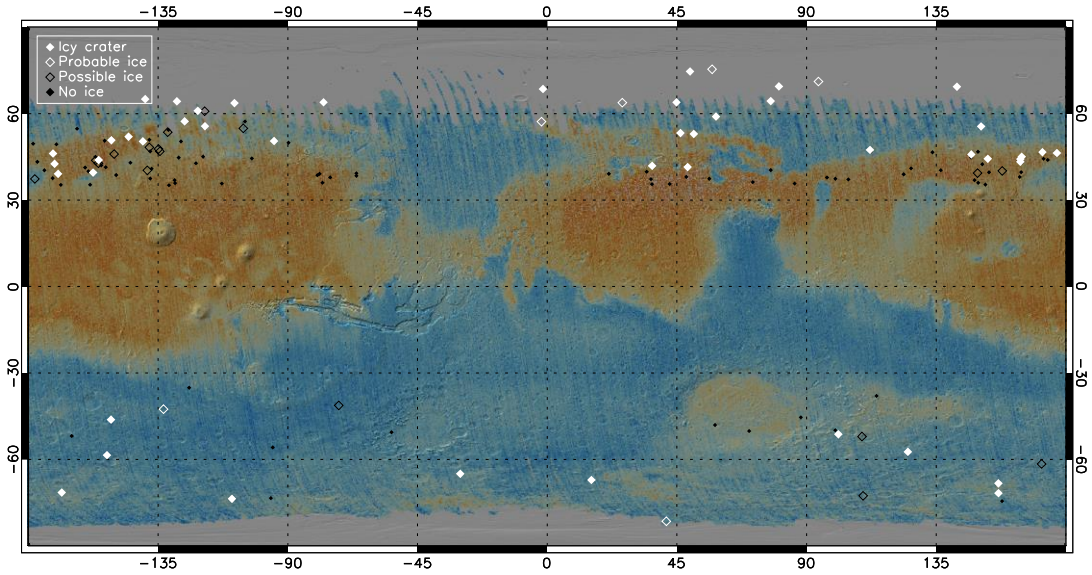

Figure 12. Map of confirmed and probable ice-exposing craters (solid and open white diamonds respectively), possible ice-exposing craters (open black diamonds), and non-ice-exposing craters (black points) poleward of 35° latitude in each hemisphere. New dated impacts equatorward of 35 °N/S are not shown in this figure. The background map is the dust-cover index map of Ruff and Christensen (2002) in simple cylindrical projection; new impact detections overall are biased towards dusty regions (orange and yellow tones) although bright ice exposure might aid crater detection in non-dusty regions.

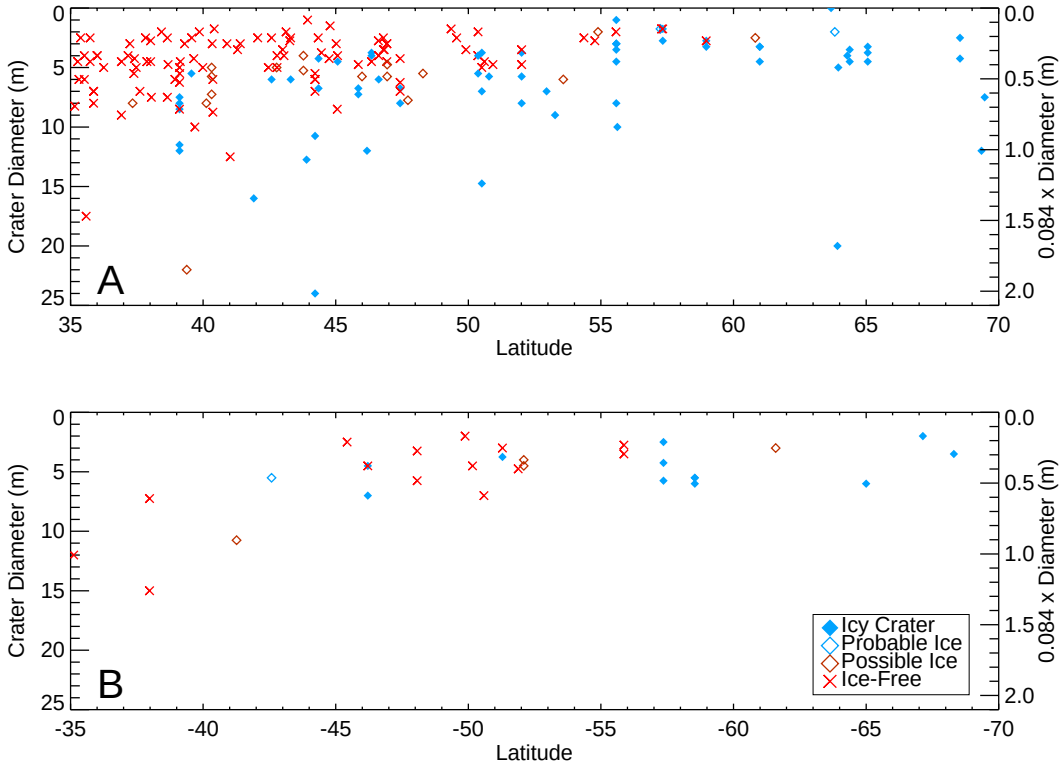

Figure 13. Plot of latitude vs. crater diameter for new impacts in the northern hemisphere (A) and southern hemisphere (B). Probable and confirmed ice-exposing craters are shown in blue. The right-hand axis shows 0.084× the crater diameter, an estimate of the maximum excavation depth. Some craters are at latitudes or diameters larger than the maximum plotted but are excluded to enhance visibility of the shallow craters and transitional latitudes. In both hemispheres the depth to ice becomes shallower at high latitude, but at latitudes where ice exists it is commonly present at a depth <1 m, consistent with ice stability theory.

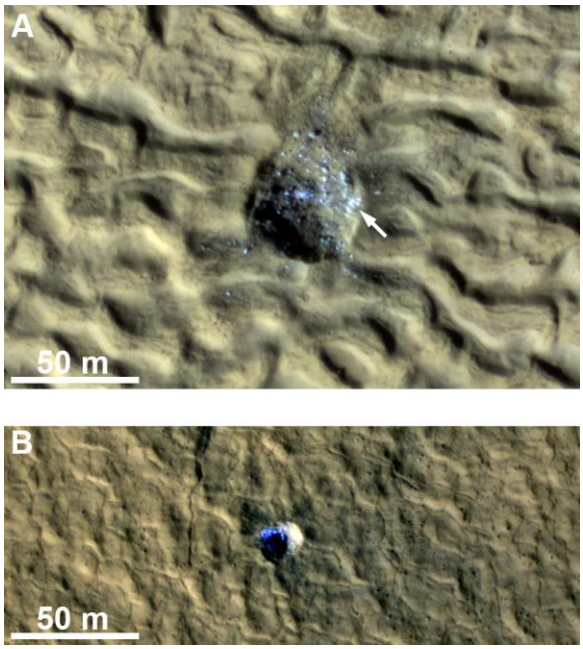

Figure 14. Ice-exposing craters in the Protonilus Mensae region. Both craters excavate blocky ice-rich material. On the east (west-facing) crater wall, ice appears to be within the core of a ridge (arrow). (A: HiRISE image ESP_046707_2220 (41.4 °N, 48.8 °E), acquired at L_S=185°. B: HiRISE image ESP_046747_2220 (41.9 °N, 36.4 °E), acquired at L_S=187°. Illumination is from the lower left in both panels.)

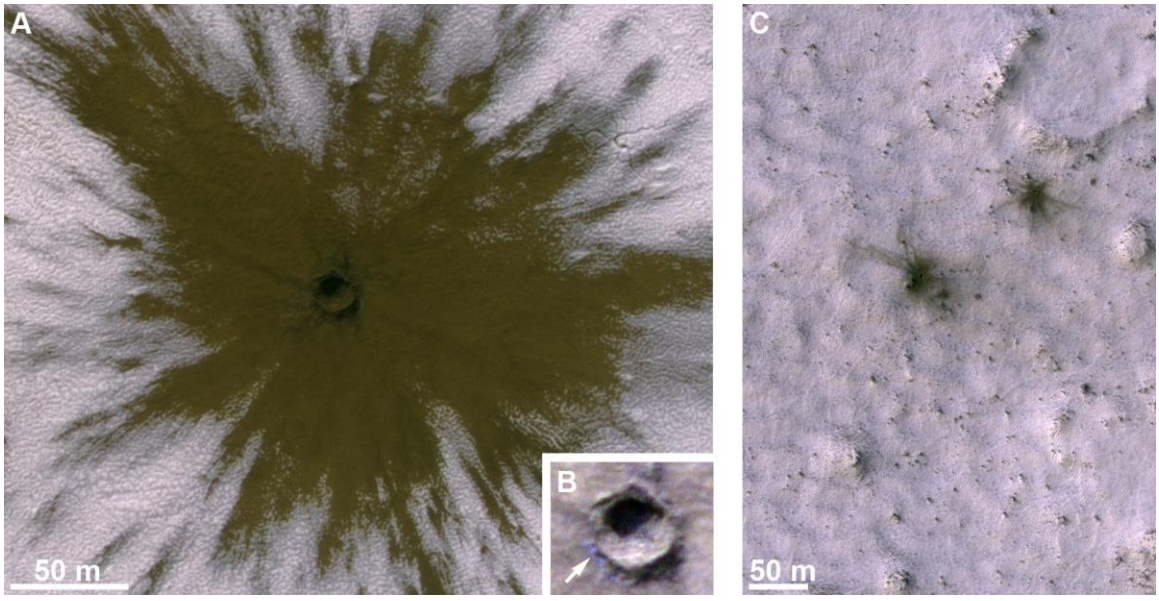

Figure 15. New impact craters with ejecta superposing seasonal frost. A) Crater on the south polar layered deposits (81.5 °S, 41.4 °E). B) The same crater (2× enlarged) after defrosting. Arrow indicates a minor exposure of relatively-blue material interpreted as probable ground ice; however, despite the ice-rich nature of the SPLD and substantial size of this crater, the distinct ice deposit is minimal even though images were acquired rapidly after formation. Note that the color stretch in this cutout is different from that in A, to emphasize relative color variations; the crater and immediate surroundings are unchanged but there is no longer frost providing a strong relative contrast. C) Small craters with ejecta superposing the seasonal CO_2 cap (55.9 °S, 264.8 °E). (A: HiRISE image ESP_057152_0985 (L_S=263°). North is towards upper right (polar stereographic projection) and illumination from the top. B: HiRISE image ESP_057574_0985 (L_S=284°). C: HiRISE image ESP_037284_1240 (L_S=159°). North is up and illumination from the upper left.)

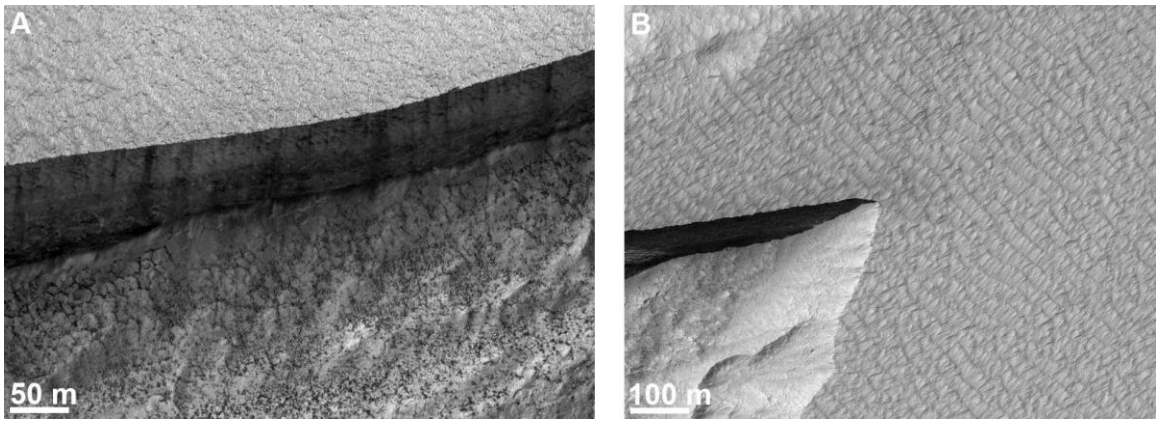

Figure 16. Possible modification processes maintaining ice exposures. A) Striations on the surface of a scarp with likely winter frost cover suggest active frost-driven mass wasting. B) Ridges on the plateau surface above southern-hemisphere scarp #3 resemble bedforms interpreted as dust accumulation features by Geissler (2014) and indicate winds

from the upper right. (A: HiRISE image ESP_064006_1245 (55.1 °S, 109.4 °E), acquired at L_S=171°. B: HiRISE image ESP_040772_1215 (58.1 °S, 93.7 °E), acquired at L_S=322°. Illumination is from the upper left in both panels.)